Analysis of Total Column CO_2 and CH_4 Measurements in Berlin with WRF-GHG

Xinxu Zhao[1], Julia Marshall[2], Stephan Hachinger[3], Christoph Gerbig[2], Matthias Frey[4], Frank Hase[4], and Jia Chen[1]

[1]Electrical and Computer Engineering, Technische Unversität München, 80333 Munich, Germany
[2]Max Plank Institute of Biogeochemistry, 07745 Jena, Germany
[3]Leibniz Supercomputing Center (Leibniz-Rechenzenturm, LRZ) of Bavarian Academy of Sciences and Humanities, Bolzmannstr. 1, 85748 Garching, Germany
[4]Karlsruhe Institute of Technology (KIT), Institute of Meteorology and Climate Research (IMK-ASF), Karlsruhe, Germany

Correspondence: Jia Chen (jia.chen@tum.de)

Abstract. Though they cover less than 3 % of the global land area, urban areas are responsible for over 70 % of the global greenhouse gas (GHG) emissions and contain 55 % of the global population. A quantitative tracking of GHG emissions in urban areas is therefore of great importance, with the aim of accurately assessing the amount of emissions and identifying the emission sources. The Weather Research and Forecasting model (WRF) coupled with GHG modules (WRF-GHG) developed for mesoscale atmospheric GHG transport, can predict column-averaged abundances of CO_2 and CH_4 (XCO_2 and XCH_4). In this study, we use WRF-GHG to model the Berlin area at a high spatial resolution of 1 km. The simulated wind and concentration fields were compared with the measurements from a campaign performed around Berlin in 2014 (Hase et al., 2015). The measured and simulated wind fields mostly demonstrate good agreement. The simulated XCO_2 shows quite similar trends with the measurement but with approx. 1 ppm bias, while a bias in the simulated XCH_4 of around 2.7 % is found. The bias can attribute to relatively high initialization values for the background concentration field and the errors in the tropopause height. We find that an analysis using differential column methodology (DCM) works well for the XCH_4 comparison, as corresponding background biases then cancel out. From the tracer analysis, we find that the enhancement of XCH_4 is highly dependent on human activities. The XCO_2 signal in the vicinity of Berlin is dominated by anthropogenic behavior rather than biogenic activities. We conclude that DCM is an effective method for comparing models to observations independently of biases caused, e.g., by initial conditions. It allows us to use our high resolution WRF-GHG model to detect and understand major sources of GHG emissions in urban areas.

1 Introduction

The share of greenhouse gas (GHG) emissions released from urban areas has continued to increase as a result of urbanization
20 (IEA, 2008; Kennedy et al., 2009; Parshall et al., 2010; IPCC, 2014). At present 55 % of the global population resides in urban
areas (UNDESA, 2014), a number that is projected to rise to 68 % by 2050 (UNDESA, 2018). Meanwhile urban areas cover
less than 3 % of the land surface worldwide (Wu et al., 2016), but consume over 66 % of the world's energy (Fragkias et al.,
2013), and generate more than 70 % of anthropogenic GHG emissions (Hopkins et al., 2016). Carbon dioxide (CO_2) emissions
from energy use in cities are estimated to comprise more than 75 % of the global energy-related CO_2, with a rise of 1.8 % per
25 year projected under business-as-usual scenarios between 2006 and 2030 (IEA, 2009). Methane (CH_4) emissions from energy,
waste, agriculture, and transportation in urban areas make up approximately 21 % of the global CH_4 emissions (Marcotullio
et al., 2013; Hopkins et al., 2016). As emission hotspots, urban areas therefore play a vital role in GHG mitigation. It is crucial
to find appropriate methods for understanding and projecting the effects of GHG emissions on urban areas, and for formulating
mitigation strategies.

30 There are two methods for the quantitative analysis of GHG emissions: the 'bottom-up' approach and the 'top-down' approach (Pillai et al., 2011; Caulton et al., 2014; Newman et al., 2016). The 'bottom-up' approach calculates emissions based
on activity data (i.e., a quantitative measure of the activity that can emit GHGs) and emission factors (Wang et al., 2009). This
approach has some uncertainty, e.g., on the national fossil-fuel CO_2 emission estimates, ranging from a few percent (e.g., 3 %-5
% for the US) to a maximum of over 50 % for countries with less resources for data collection and poor statistical framework
35 (Andres et al., 2012). The considerable uncertainties are caused by the large variability of source-specific and country-specific
emission factors and the incomplete understanding of emission processes (Montzka et al., 2011; Bergamaschi et al., 2015).
These uncertainties grow larger at sub-national scales, when estimating the disaggregation of the national annual totals in
space and time. The 'top-down' approach can not only provide estimated global fluxes, but also verify the consistency and assess the uncertainties of bottom-up emission inventories (Wunch et al., 2009; Montzka et al., 2011; Bergamaschi et al., 2018).
40 However, it is hard to quantify the statistical errors attached to both atmospheric observations and prior knowledge about the
distribution of emissions and sinks (Cressot et al., 2014).

McKain et al. (2012) suggested that column measurements can provide a promising route to improving the detection of CO_2
emitted from major source regions, possibly avoiding extensive surface measurements near such regions. Such measurements,
i.e. measurements of concentration averaged over a column of air, are performed to help to disentangle the effects of atmo-
45 spheric mixing from the surface exchange (Wunch et al., 2011) and decrease the biases associated with estimates of carbon
sources and sinks in atmospheric inversions (Olsen and Randerson, 2004). Compared to surface values, urban enhancements
in columns are less sensitive to boundary-layer heights (Wunch et al., 2011; McKain et al., 2012; Kivi and Heikkinen, 2016)
and column observations have the potential to mitigate mixing height errors in an atmospheric inversion system (Gerbig et al.,
2008). Atmospheric GHG column measurements combined with inverse models are thus a promising method for analyzing
50 GHG emissions, and can be used to analyze their spatial and temporal variability (Ohyama et al., 2009; Pillai et al., 2011;
Ostler et al., 2016; Kivi and Heikkinen, 2016).

In order to focus the 'top-down' approach on concentration differences caused by local and regional emission sources, and in particular to quantify urban emissions, the differential column methodology (DCM) was proposed. It evaluates differences between column measurements at different sites. Chen et al. (2016) applied the DCM using compact Fourier Transform Spectrometers (FTS) EM27/SUN (Bruker Optik, Germany) and demonstrated the capability of differential column measurements for determining urban and local emissions in combination with column models. Citywide GHG column measurement campaigns have been carried out, e.g., in Boston (Chen et al., 2013), Indianapolis (Franklin et al., 2017), San Francisco, Berlin (Hase et al., 2015), and Munich (Chen et al., 2018). However, only a few studies have combined differential column measurements with high-resolution models. Toja-Silva et al. (2017) simulated the column data at upwind and downwind sites of a gas-fired power plant in Munich using the Computational Fluid Dynamic model (CFD) and compared them with the column measurements. Viatte et al. (2017) quantified CH_4 emissions from the largest dairies in the southern California region, using four EM27/SUNs in combination with the Weather Research and Forecasting model (WRF) in large-eddy simulation mode. Vogel et al. (2019) deployed five EM27/SUN in the Paris metropolitan area and analyzed the data with the atmospheric transport model framework CHIMERE-CAMS.

This paper carries out a quantitative analysis of GHG for the Berlin area in combination with DCM. We utilize the mesoscale WRF model (Skamarock et al., 2008) coupled with GHG modules (WRF-GHG) (Beck et al., 2011) at a high resolution of 1 km. The aim is to assess the precision of WRF-GHG and to provide insights on how to detect and understand sources of GHGs (CO_2 and CH_4) within urban areas. WRF is a numerical weather prediction system and can be used for both atmospheric research and operational forecasting, on a mesoscale range from tens of meters to thousands of kilometers, cf. e.g. (Chen et al., 2011). To produce high-resolution regional simulations of atmospheric CH_4 passive tracer transports, WRF was coupled with the Vegetation Photosynthesis and Respiration module (WRF-VPRM) (Ahmadov et al., 2007). WRF-VPRM has been widely employed in several studies, in which both the generally good agreement of the simulations with measurements and model biases have been assessed in detail (Ahmadov et al., 2009; Pillai et al., 2011, 2012; Kretschmer et al., 2012). Biogenic carbon fluxes given by the VPRM model tend to underestimate urban ecosystem carbon exchange, owing to the incomplete understanding of urban vegetation, and to conditions related to urban heat islands and altered urban phenology (Hardiman et al., 2017). WRF-VPRM was later extended to WRF-GHG (Beck et al., 2011), which can simulate the regional passive tracer transport for GHGs (CH_4, CO_2 and carbon monoxide (CO)). Relatively few studies using WRF-GHG have been published as yet. Pillai et al. (2016) utilized a Bayesian inversion approach based on WRF-GHG at a high spatial resolution of 10 km for Berlin to obtain anthropogenic CO_2 emissions, and to quantify the uncertainties in retrieved anthropogenic emissions related to instruments (e.g. CarbonSat) and modelling errors. In the present paper, our focus is on a high-resolution (1 km) study of both CO_2 and CH_4 in Berlin, and assess the performance of WRF-GHG through comparing the simulated wind and concentration fields to observations from wind stations and ground-based solar-viewing spectrometers. Then DCM is tested as a proper approach for model analysis, which can cancel out the bias from initialization conditions and highlight regional emission tracers. The simulation workflow is also adapted to this purpose where needed. This study is the fundamental study of the WRF-GHG mesoscale modeling framework in urban areas.

The total annual CO_2 emissions of Berlin (21.3 million tonnes in 2010) approximately correspond to those of Croatia, Jordan or the Dominican Republic (Reusswig and Lass, 2014). With its strong regulatory influence as a 'state' within Germany, and a strongly supportive policy, Berlin has already transformed itself into a climate-friendly city in which CO_2 emissions have been reduced by a third compared with 1990 levels, aiming for carbon neutrality by 2050 (Homann, 2018). Berlin therefore needs to assess and identify the emission sources accurately at the current stage, to provide solid scientific support for the selection of mitigation options. Additionally, Berlin is an ideal pilot case for developing and testing simulations because the city is relatively isolated from other large cities with high emissions, such that anthropogenic GHG anomalies around Berlin can confidently be attributed to the city itself.

The major goals of our work in this context are: (1) to simulate high-resolution (1 km) CO_2 and CH_4 concentrations for Berlin using WRF-GHG, attributing the changes in concentrations to different emission processes; (2) to compare the simulation outputs with the observations from a column measurement network in Berlin (Hase et al., 2015), assessing the precision of WRF-GHG; (3) to use DCM in the simulation analysis, testing the feasibly of this approach. The structure of this paper is as follows: The model with its domain and external data sources are described in Sect.2. A comparison analysis for wind fields and concentration fields is presented in Sect.3, and CO_2 and CH_4 concentrations related to different processes (e.g., the anthropogenic component) are discussed. DCM for the comparison of concentration fields and the tracer analysis is presented and discussed in Sect.4. Section 5 provides the discussion and summary of this study.

2   WRF-GHG Modeling System

As mentioned in Sect.1, we use the WRF model Version 3.2 coupled with GHG modules to quantify the uptake and emission of atmospheric GHGs around Berlin at a high resolution of 1 km. WRF follows the fully compressible nonhydrostatic Euler equations (Skamarock et al., 2005, 2008) and is based on the actual meteorological data in this case study. The meteorological initial conditions and lateral boundary conditions were taken from the Global Forecast System (GFS) model reanalysis in which in-situ measurements and satellite observations have been assimilated. Tracers in WRF-GHG are transported online in a passive way, i.e. without any chemical loss or production, when the tracer transport option is used (Ahmadov et al., 2007; Beck et al., 2011). As shown in Fig.1, three domains are set up here, whose dimensions are 70×50 horizontal grid points with a spacing of 9 km for the coarsest domain (d01), 3 km for the middle domain (d02) and 1 km for the innermost domain (d03). WRF uses a terrain-following hydro-static pressure vertical coordinate (Skamarock et al., 2008). In our case, 26 vertical levels are defined from the surface up to 50 hPa, 14 of which are in the lowest 2 km of the atmosphere. The innermost domain, d03, envelops all five measurement sites (see Sect.3.1) to assess the simulation by comparing with the measured data. Berlin lies in the North European Plain on flat land (crossed by northward-flowing watercourses), which avoids the vertical interpolation problems caused by topography differences (Fig.1). The Lambert conformal conic projection is selected as map projection. The simulated time span is from 18 UTC on 30th June to 00 UTC on 11th July in 2014. The description of the workflow for running WRF-GHG can be found in Appendix A.

The meteorological fields are obtained from the Global Forecast System model (GFS) at a horizontal resolution of 0.5° with 64 vertical layers and a temporal resolution of 3 hours (as available via the NOAA-NCDC/NCEI, www.ncdc.noaa.gov).

120 The GFS uses hydrostatic equations for the prediction of atmospheric conditions, and its output includes large amounts of atmospheric and land-soil variables, wind fields, temperature, precipitation and soil moisture etc. The initial and lateral boundary conditions for our WRF-GHG concentration fields are implemented using Copernicus Atmosphere Monitoring Service (CAMS) data (Agusti-Panareda et al., 2017). CAMS provides the estimated mixing ratios of CO_2 and CH_4 with a spatial resolution of 0.8° on 137 vertical levels, with a temporal resolution of 6 hours (as available via https://atmosphere.copernicus.eu).

125 The simulation of CO_2 and CH_4 fluxes with different emission tracers in WRF-GHG is based on flux models and emission inventories which are either already implemented inside the model modules ('online' calculation) or constitute external datasets ('offline' calculation). The flux values from external emission inventories are converted into atmospheric concentrations and added to the corresponding tracer variables. In combination with the background concentration fields for CO_2 and CH_4 that refer to the CO_2 and CH_4 values without any sources and sinks in the targeted domain, the tracer contributions are summed up

130 to obtain the total concentrations, as

$$CO_{2,\text{total}} = CO_{2,\text{bgd}} + CO_{2,\text{VPRM}} + CO_{2,\text{anthro}} + \Delta CO_2$$
$$CH_{4,\text{total}} = CH_{4,\text{bgd}} + CH_{4,\text{anthro}} + CH_{4,\text{soil}} + \Delta CH_4$$
(1)

where $CO_{2,\text{total}}$ and $CH_{4,\text{total}}$ represent the total CO_2 and CH_4, $CO_{2,\text{bgd}}$ and $CH_{4,\text{bgd}}$ are the background CO_2 and CH_4, $CO_{2,\text{anthro}}$ and $CH_{4,\text{anthro}}$ stand for the changes in CO_2 from the anthropogenic emissions, $CO_{2,\text{VPRM}}$ is the change in CO_2 from the biogenic activities and $CH_{4,\text{soil}}$ is the change in CH_4 from soil uptake, ΔCO_2 and ΔCH_4 are the tiny computational errors for CO_2 and

135 CH_4 described in detail in Appendix B. In the transport process, the relationship shown in Eq.1 holds for each vertical level.

The biogenic CO_2 emission is calculated online using VPRM (Mahadevan et al., 2008), in which the hourly Net Ecosystem Exchange (NEE) of CO_2 reflects the biospheric fluxes between the terrestrial biosphere and the atmosphere, estimated by the sum of Gross Ecosystem Exchange (GEE) and Respiration. VPRM in WRF-GHG calculates biogenic fluxes initialized by vegetation indexes (land surface water index (LSWI), enhanced vegetation index (EVI), etc..) from the MODIS satellite

140 (as available via https://modis.gsfc.nasa.gov/). Combined with SYNMAP vegetation classification at a resolution of 1 km, the refectance data from the MODIS satellite at a 500-m spatial resolution and 8-day intervals is aggregated to the Lambert Conformal Conic (LCC) projection within the WRF-VPRM preprocessor. Then, the data including these high-solution vegetation indexes at a resolution of 1 km are available on the model domains.

We use the external dataset Emission Database for Global Atmospheric Research Version 4.1 (EDGAR V.4.1) for the anthro-

145 pogenic fluxes in our study. EDGAR V.4.1 provides annually varying global anthropogenic GHG emissions and air pollutants at a spatial resolution of 0.1° (Muntean et al., 2014; Janssens-Maenhout et al., 2015), whose source sectors include industrial processes, on-road and off-road sources in transport, large-scale biomass burning and other anthropogenic sources (Saikawa et al., 2017). Here we apply time factors for seasonal, weekly, daily and diurnal variations defined by the time profiles published on the EDGAR website (http://themasites.pbl.nl/tridion/en/themasites/edgar/documentation/content/Temporal-variation.html);

150 however, considerable uncertainties are to be expected in applying these time factors. This temporal variation set is derived

based on western European data such that the representativity for other European countries and even other world regions may be quite poor. The coarse emission fluxes used for the initialization of the anthropogenic tracer in WRF-GHG can cause problems when locating emission points within the high-resolution model grid, and can weaken the impact from the real high emission hot-spots in the fine domain of our study. The chemical sink for atmospheric CH_4 (e.g., photo-chemistry in the stratosphere) can be ignored in the model owing to its relatively long lifespan (9.5 ± 1.3 year, Holmes (2018)), the small-scale domains, and the limited simulation period (10 days) in our case.

3 Model Analysis and Model-Measurement Comparison

3.1 Description of Measurement Sites

The measurement campaign used to compare with WRF-GHG in this paper was performed from 23rd June to 11th July 2014 in Berlin using five spectrometers (Hase et al., 2015). It allows us to both test the precision of WRF-GHG (Sect.3) and verify differential column methodology (DCM) as our analytic methodology (Sect.4). In their measurement campaign, Hase et al. (2015) used five portable Bruker EM27/SUN Fourier Transform Spectrometers (FTS) for atmospheric measurements based on solar absorption spectroscopy. Five sampling stations around Berlin were set up, four of which (Mahlsdorf, Heiligensee, Lindenberg and Lichtenrade) were roughly situated along a circle with a radius of 12 km around the center of Berlin. Another sampling site was closer to the city center and located inside the Berlin motorway ring at Charlottenburg (Fig.6). Detailed information on this measurement campaign is given in Hase et al. (2015) and Frey et al. (2015) provides additional details on the calibration of the spectrometers, precision and instrument-to-instrument biases.

3.2 Comparison of Wind Fields at 10 meters

Winds have a strong impact on the vertical mixing of GHGs and a direct influence on their atmospheric transport patterns. Hence, we firstly compare the wind speeds and wind directions obtained from WRF-GHG to the measurements, such that deviations between the simulated and measured wind fields are assessed. The wind measurements are not exactly co-located with the spectrometers mentioned in Sect.3.1, but rather are located at three sampling sites (Tegel, Schönefeld and Tempelhof, respectively) and measure at a height of 10 meters above the ground. The simulated wind speed at 10 meters (ws_{10m}) and wind direction at 10 meters (wd_{10m}) are calculated following the equations,

$$
\begin{aligned}
ws_{10\text{m}} &= \sqrt{u_{10\text{m}}^2 + v_{10\text{m}}^2} \\
wd_{10\text{m}} &= \arctan \frac{v_{10\text{m}}}{u_{10\text{m}}}
\end{aligned}
\tag{2}
$$

where $u_{10\text{m}}$ and $v_{10\text{m}}$ are the components of the horizontal wind, towards the east and north respectively, which can be obtained from WRF-GHG output files.

Figure.2 shows the comparisons of wind speeds (Fig.2(a)) and wind directions (Fig.2(b)) between simulations and observations at 10 meters from 1st July to 10th July and the model-measurement differences. EM27/SUN only operates in the daytime

180 under enough sunlight (the detailed description of the instrument can be found in Gisi et al. (2012), Frey et al. (2015) and Vogel et al. (2019)). The instrumental working periods are marked by gray shaded boxes in Fig.2. The measured (dashed lines) and simulated (solid) wind speeds (Fig.2(a)) at 10 meters show similar trends and demonstrate relatively good agreement over the 10-day time series with a root mean square error (RMSE) of $0.9247\,\mathrm{m/s}$. Large uncertainties in wind speeds are found to appear always with the lower wind speeds, mostly at night. In terms of wind directions at 10 meters, we observe that the sim-

185 ulated wind directions show similar but slightly underestimated fluctuations (Fig.2(b)), which result in a RMSE of $60.8328°$. Larger uncertainties in wind directions always exist during the low wind speed periods (Fig.2(a)&(b)). During the instrumental working period (within the daytime), the simulations fit better with the measurements with relatively lower RMSEs $0.6928\,\mathrm{m/s}$ for wind speeds and $41.4793°$ for wind directions. We find that the measured wind fields (both wind speeds and wind directions) have more fluctuations, compared to the simulations. This could be caused by real fast wind changes, which the model,

190 simulating a somewhat idealized environment, is not able to capture. To be specific, local turbulence given by urban canopy, buildings etc. are not represented well in the model.

3.3 Comparison of pressure-weighted column-averaged concentrations

In the following, we use the measured concentration fields to compare with the simulated fields. An FTS EM27/SUN can measure the column-integrated amount of a tracer through the atmospheric column with excellent precision, yielding the

195 column-averaged dry-air mole fractions (DMFs) of the target gases (Chen et al., 2016; Hedelius et al., 2016). The measured DMFs of CO_2 and CH_4 are denoted by XCO_2 and XCH_4. Hase et al. (2015) used constant a priori profile shapes in the retrievals of measurements.

When comparing remote sensing observations to model data (or also datasets from different remote sensing instruments to one another), limitations of the instruments in reconstructing the actual atmospheric state need to be taken into account.

200 In general, this requires the a-priori profile which was used for the retrieval and the averaging kernel matrix, which specifies the loss of vertical resolution (fine vertical details of the actual trace gas profile cannot be resolved) and limited sensitivity (e.g. Rodgers and Connor (2003)). In the case of EM27/SUN, the spectrometers used be the network offer only a low spectral resolution of $0.5\,\mathrm{cm^{-1}}$. Therefore, performing a simple least squares fit by scaling retrieval of the a-priori profile is generally appropriate. In this case, there is no need to specify a full averaging kernel matrix, instead, the specification of a total column

205 sensitivity is sufficient. The total column sensitivity is a vector (being a function of altitude), which specifies to which degree an excess partial column superimposed on the actual profile at a certain input altitude is reflected in the retrieved total column amount. This sensitivity vector is a function of solar zenith angle (and ground pressure), mainly due to the fact that the observed signal levels in different channels building the spectral scene used for the retrieval are shaped by a mixture of weaker and stronger absorptions (if all spectral lines in the spectral scene would be optically thin and too narrow to be resolved by the

210 spectral measurement, the sensitivity would approach unity throughout).

In order to ensure measurement qualities and enough sample points for further concentration comparisons, we select five measurement dates (1st, 3rd, 4th, 6th and 10th July) with relatively good measurement qualities (from fair '++' to very good '++++') based on Hase et al. (2015). The pressure-dependent column sensitivities for CO_2 (Fig.3(b)) and CH_4 (Fig.3(c))

are derived from measurements performed in Lindenberg on 4th July (the best measurement-quality day). Details about the measurements can be found in Hase et al. (2015) and Frey et al. (2015). The shape and values of the column sensitivities from Karlsruhe closely resemble the results of Hedelius et al. (2016) in Pasadena. As depicted in Fig.3(a), the solar zenith angles (SZAs) are almost identical for each day in our study (at each hour), rendering the shape of column sensitivities (at a specific hour of the day) practically independent of the measurement date. The column sensitivities for 4th July (Fig.3(b,c)), are taken as a basis for our smoothing process below. The a-priori CO_2 and CH_4 profiles are taken from the Whole Atmosphere Community Climate model (WACCM) Version 6. A smoothed profile for a target gas G is then obtained as Eq.3 in (cf. Vogel et al., 2019),

$$G^s = K * G + (I - K) * G^p \tag{3}$$

where G is the modelled profile from WRF-GHG for a target gas G, I is the identity matrix, K is a diagonal matrix containing the averaging kernel, and G^p is the a-priori profile.

In order to compare the simulated smoothed concentration fields with the observations, the simulated smoothed pressure-weighted column-averaged concentration for a target gas G (XG) is calculated as,

$$\Delta p(i) = \frac{P(i) - P(i+1)}{P_{\text{sf}} - P_{\text{top}}} \rightarrow XG = \sum_{i=1}^{n} \Delta p(i) \times G^s(i) \tag{4}$$

Here, Δp_i is the proportional to the differences of the pressure values $P(i)$ at the bottom and $P(i+1)$ at the top of the ith vertical grid cell; P_{top} and P_{sf} represent the hydrostatic pressures at the top and at the surface of the model domain, and $G^s(i)$ stands for the simulated concentration of the target gas G at the ith vertical level.

In Figures.D1 and D2 of Appendix D, we compare the simulated XCO_2 and XCH_4 with and without smoothing. The simulated concentrations are only slightly enlarged after smoothing, approximately 1-2 ppm for XCO_2 and 2 ppb for XCH_4, while the variations are mostly not changed. Compare to the period with lower SZAs (at noon), the smoothed values in the morning and afternoon with higher SZAs hold relatively larger enlargements.

Figure.4(a) shows the measured and modelled variations of XCO_2 and XCH_4 for these five days. Compared to the measurements, the smoothed simulated pressure-weighted column-averaged concentrations for CO_2 (XCO_2) show quite similar trends but with approx. 1-2 ppm bias, indicated by a RMSE of 1.2534 ppm. The simulated XCO_2 are overestimated for 1st, 3rd and 4th July while on 6th and 10th July, the model is underestimated, which could attribute to the uncertainties from the coarse anthropogenic surface emission fluxes, background concentrations from CAMS (Sembhi et al., 2015), and the ignorance of the influence from the line of the sun sight.

Figure.4(b) shows the comparison of the pressure-weighted column-averaged concentrations for CH_4 (XCH_4) between observations and smoothed simulations on the five selected dates (1st, 3rd, 4th, 6th and 10th July). We find that there is an approximate offset of 50-60 ppb between observations and models (RMSE = 58.1082 ppb). The simulated XCH_4 is around 1860 ppb while the measured value is around 1810 ppb which is comparable to the values (1790-1810 ppb) observed at two Total Carbon Column Observing Network (TCCON) measurement sites in June and July 2014, Bremen in Germany (Notholt et al., 2014) and Bialystok in Poland (Deutscher et al., 2014). This bias of the simulated XCH_4 seems to be constant (around 2.7 %) each day. Thus, we introduce an offset applied to all sites for each simulation date to compare the model and the measured

data, effectively removing the bias, which we attribute to a too high background XCH_4. The daily offset is assumed to be the difference between the simulated and measured daily mean XCH_4. After applying the daily offset, the measured XCH_4 shows a somewhat better agreement and a similar trend but with larger variability, compared to the simulation (RMSE = 3.1690 ppb). The smaller variations from the simulation results can, e.g., be caused by the error from the spatial-temporal treatment of emission maps, underestimated emissions from anthropogenic activities, the coarse wind data and/or the smoothing of actual extreme values in the simulation.

A major offset in modelled CH_4 concentration fields could potentially be attributed to the errors in the troposphere height and a general offset from CAMS. In the CH_4 vertical concentrations profile, we find that the typical sharp decrease is given within the tropopause height. Tukiainen et al. (2016) also find the similar sharp decrease when using the air-cores to retrieve the atmospheric CH_4 profiles in Finland. During the simulation, the background concentration values of CAMS are directly fitted to the WRF pressure axis, without the consideration of the actual tropopause height, thus this is unlikely to be the case. An illustration of the vertical distribution for CH_4 is provided in Appendix C. While the CO_2 vertical distribution shows a quite flat decrease with the increase of pressure and there is no need to consider the tropopause height during the grid treatment in the vertical layer. Then in view of CAMS, the reports from Monitoring Atmospheric Composition and Climate (MACC) described that CAMS held an increase of bias and RMSE (approx. 50 ppb) in each part of the world, compared to the Integrated Carbon Observation System (ICOS) observations in 2017 (Basart et al., 2017). Galkowski et al. (2019) also mentioned one CH_4 offset (approx. 30 ppb within troposphere), when initializing the concentration fields using CAMS. Apart from these two major potential reasons for the bias, the influence from the in-accurate simulated planetary boundary layers and the shape of the constant a priori profile used for the retrievals both potentially contribute to the discrepancies for the concentration fields. Due to the lack of fine measured vertical concentration profiles, it is not easy to quantify these errors and attribute these potential reasons to this 2.7% error quantitatively. Thus, a DCM-based analysis is presented in Sect.4, aiming at eliminating the bias from these relatively high initialization values for CH_4 and making it easier to assess WRF-GHG results with respect to the measurements.

3.4 Contributions of different sources and sinks to the total signal: Individual Emission Tracers

As described in Sect.2, the various flux models implemented in WRF-GHG are advected as separate tracers, making it possible to distinguish the signals in concentration space for different source and sink categories for CO_2 and CH_4 (Beck et al., 2011). Berlin is located in an area of low-lying, marshy woodlands with a mainly flat topography (Kindler et al., 2018). There is no wetland in Berlin according to the MODIS Land Cover Map (Friedl et al., 2010). The land covered by forests, green and open spaces (e.g., farmlands, parks, allotment gardens) accounts for 35 % of the total area in Berlin (SenStadtH, 2016). Additionally, eleven power plants are currently being operated in Berlin, eight of which have a capacity over 100 MW (Fraunhofer-Gesellschaft, 2018). In accordance with the geographical characteristics of the district and potential emission sources in Berlin, we focus on understanding the major emissions caused by vegetation photosynthesis and respiration ($XCO_{2,VPRM}$) as well as anthropogenic activities ($XCO_{2,anthro}$) for CO_2, and by soil uptake ($XCH_{4,soil}$) as well as human activities ($XCH_{4,anthro}$) for CH_4.

As an instructive example of an analysis involving these tracers, we look at the diurnal cycle of contributions from the different tracers mentioned above in Charlottenburg (Fig.5). The mean values, averaged over 9 days (from 2nd to 10th July) as well as a 95 % confidential interval calculated in the averaging process are shown in Fig.5. Figure.5(a) clearly shows a decline during the day and a rise at night in the XCO_2 enhancement over the background (blue: $XCO_{2,total}$ - $XCO_{2,bgd}$),

285 with a maximum decrease over the course of the day of around 2 ppm. The XCO_2 enhancement over the background reaches its daily peak during morning rush hour (07 UTC). The morning peak corresponds to XCO_2 changes from human activities, depicted by the black line from 04 UTC to 07 UTC (marked by a red square in Fig.5(a)). Before the evening rush hour (16 UTC), XCO_2 over the background then decreases, owning to biogenic uptake. Beginning in the evening, values increase again. The fluctuation in the evening (17 UTC – 19 UTC) are dominated by XCO_2 enhancements from human activities while

290 the substantial rise from 19 UTC onward is generated by the VPRM tracer, specifically the accumulation of the vegetation respiration in the evening.

XCO2 is weaker compared to the strong biogenic uptake. To further highlight the role of anthropogenic activities in XCO_2 changes within the urban area, DCM is applied in Sect.4. More specifically, we will use downwind-minus-upwind column differences of CO_2 (ΔXCO_2) to describe the XCO_2 enhancement over an upwind site, as the difference between the downwind

295 and upwind sites can be attributed to urban emissions.

Turning to XCH_4 in Fig.5(b), we plot the variations of the mean hourly contributions from the anthropogenic (black line: $XCH_{4,anthro}$) and soil uptake tracer (blue: $XCH_{4,soil}$) in Charlottenburg. The contributions by anthropogenic activities fluctuate slightly around 2 ppb in the morning and at noon; then a peak occurs at the start of the evening rush hour (16 UTC). After 18 UTC, values clearly decrease, reaching approximately 2 ppb. From 21 UTC XCH_4 stabilizes, exhibiting only moderate

300 fluctuations. The XCH_4 enhancement above the background (green: $XCH_{4,total}$ - $XCH_{4,bgd}$) depends largely on the XCH_4 contributions by human activities. The changes in concentrations caused by the soil uptake tracer (blue), whose values fluctuate between 0.001 ppb and 0.01 ppb, have almost no influence on the variation of the XCH_4 enhancement over background in the urban area.

4 Model Analysis using Differential Column Methodology

305 ### 4.1 Comparison of differential column concentrations

The differential column methodology (DCM) can be employed to detect and estimate local emission sources within an area, based on calculated concentration differences between downwind and upwind sites (Chen et al., 2016). The difference (ΔXG) of a specific gas G in column-averaged DMFs across the downwind and upwind sites is defined as,

$$\Delta XG = XG_{\text{downwind}} - XG_{\text{upwind}} \tag{5}$$

310 where XG_{downwind} and XG_{upwind} represent the column-average DMFs at the downwind and upwind sites.

In this study, DCM is applied to measurements and models in the spirit of a post-processing analysis. This approach is not only useful to cancel out the bias of the simulated XCH_4 (see Sect.3.3), but also to assess the role of anthropogenic activities in XCO_2 changes more appropriately.

A necessary prerequisite for DCM is distinguishing the upwind and downwind sites among all five sampling sites. Wind direction thus plays a pivotal role in the calculation of the downwind-minus-upwind column differences. In this study, the hourly simulated vertical-averaged wind directions are assumed as a standard to classify the sites into downwind and upwind sites. The tracer transport calculations in the first few hours are not stable in WRF-GHG. Thus, we select 3rd, 4th, 6th and 10th as our targeted dates.

Table.1 shows the daily average wind directions with standard derivations and the details on the downwind and upwind sites for these four target dates. West wind is the prevailing wind direction on 3rd. That is to say, Mahlsdorf and Lindenberg are downwind sites, and the upwind sites corresponding to these are Charlottenburg and Heiligensee. While the wind on 10th July is northeasterly and the combination of downwind and upwind sites are selected to be opposite of the ones on 3rd July. The prevailing wind on 4th and 6th are easterly. The upwind site is Lichtenrade, and the corresponding downwind sites are Heiligensee and Lindenberg. Based on the selection of downwind and upwind sites shown in Table.1 and Eq.5, differential column concentrations (ΔXCH_4) are, therefore, respectively, calculated as:

$$\text{West Wind (3rd July)} : \Delta XCH_4 = (XCH_4^{\text{Mahlsdorf}} + XCH_4^{\text{Lindenberg}})/2 - (XCH_4^{\text{Charlottenburg}} + XCH_4^{\text{Lichtenrade}})/2 \tag{6}$$

$$\text{North Wind (4th and 6th July)} : \Delta XCH_4 = (XCH_4^{\text{Heiligensee}} + XCH_4^{\text{Lindenberg}})/2 - XCH_4^{\text{Lichtenrade}} \tag{7}$$

$$\text{Northeast Wind (10th July)} : \Delta XCH_4 = (XCH_4^{\text{Charlottenburg}} + XCH_4^{\text{Lichtenrade}})/2 - (XCH_4^{\text{Mahlsdorf}} + XCH_4^{\text{Lindenberg}})/2 \tag{8}$$

Figure.7 depicts the variations of the wind fields (wind speeds and wind directions) and ΔXCH_4 (corresponding to Eq.6, 7 and 8) on 3rd, 4th, 6th and 10th July. As depicted in the left column of Fig.7, the hourly vertical-mean simulated wind speeds and directions at downwind and upwind sites are homogeneous. Thus, it is reasonable to use the daily mean wind directions as the standard for the selection of downwind and upwind sites. The general trends in the simulated ΔXCH_4 values, shown in the right column of Fig.7, seem to be roughly reproduced by the observations but slightly overestimated, with a RMSE of $1.3895\,\text{ppb}$.

Yet, DCM as presented here has potential to highlight the role of anthropogenic activities, which we demonstrate applying it to CO_2 tracers in the simulation. Thus, the analysis on anthropogenic and biogenic tracers for CO_2 will be specially prominent here. As described above, we continue to take 3rd, 4th, 6th and 10th July as examples (see the left column of Fig. 8).

With the left column of Fig.8, the variations of ΔXCO_2 (corresponding to Eq.6, 7 and 8) on 3rd, 4th, 6th and 10th are shown. In contrast to XCO_2 values (Sect.3.4, Fig.5(a)), the simulated ΔXCO_2 (Fig.8, left column, blue lines) is not so much influenced by the XCO_2 changes from the VPRM tracer (Fig.8, left column, green), but more closely follows the XCO_2 changes from anthropogenic activities (Fig.8, left column, red). With DCM, the role of human activities in XCO_2 changes is highlighted and the strong effect from the biogenic component is canceled out. The ΔXCO_2 measurements (Fig.8, left column, black) show similar trends as the simulation with a RMSE of $0.2973\,\text{ppm}$.

To further understand the differences of ΔXCO_2 and ΔXCH_4 between measurements and simulations (see Fig.7, right
345   column and Fig.8, left column), the comparisons of hourly mean ΔXCO_2 and ΔXCH_4 values for these four targeted dates
are illustrated in the right column of Fig.8. Due to the restriction of measured wind information, we illustrate the differences
of simulated and measured wind directions at 10 meters (i.e. Fig.2(b)) with respect to the hourly mean ΔXCO_2 and ΔXCH_4.
We find that the real hourly mean ΔXCO_2 and ΔXCH_4 values are generally higher than the simulated values. Extreme points
are colored red and blue in the right column of Fig.8, standing for large differences between measured and simulated wind
350   directions at 10 meters. We see that a large difference of wind directions is a necessary but insufficient condition for the bias
of ΔXCO_2 and ΔXCH_4 between measurements and simulations. In future studies, this is suggested to be verified further.

We conclude that DCM, as applied in this plot, reduces the model bias caused by the simulation initialization, but introduces
unpleasant effects which may be attributed to errors in the assumed or simulated wind directions.

4.2   Comparison between differential column concentrations and modeling results after the elimination of wind
355   influence

As described in Sect.4.1, the wind direction impacts the distinction between downwind and upwind sites for DCM. Devising
meaningful and accurate recipes for determining the wind directions is not easy, sometimes resulting in mixed-quality results
(of Sect.4.1). Our simulated output provides the hourly wind and concentration fields. The instruments measure the concentra-
tion value every minute (Hase et al., 2015) We simply assume the wind direction to be a constant value within one hour (the
360   hourly vertical-averaged values) in our calculation, also when it comes to selecting up- and downwind sites. This may create
inaccuracies in the calculation of the measured ΔXCH_4.

In this section, we test replacing the upwind values in DCM by an all-site mean to provide a potential solution for the
elimination of such problems while still applying the DCM. The mean of the column-averaged DMFs over all sampling sites
($\overline{XG}_{\text{specific site}}$) is assumed to be the background concentration within the entire urban region, replacing the XCH_4 at the upwind
365   site. The differences between the specific site and the mean of all the sites for each gas G ($\Delta\overline{XG}_{\text{specific site}}$) is then evaluated,
i.e.

$$\Delta\overline{XG}_{\text{specific site}} = XG_{\text{specific site}} - \overline{XG}_{\text{all sites}} \tag{9}$$

where $XG_{\text{specific site}}$ is the column-averaged DMF at the respective sampling site.

We now test this form of DCM for the same four targeted dates (3rd, 4th, 6th and 10th July). The distance between any two
370   sampling sites is around 25 km. The general trends of the simulated (Fig.9, blue lines) and measured (Fig.9, black) $\overline{\Delta XCH_4}$
appear to be more similar with a RMSE of $0.6698\,\text{ppb}$, compared to the comparison of ΔXCH_4 in the right column of Fig.7
(RMSE=$1.3895\,\text{ppb}$). The measurement-model bias can be caused by underestimated emissions from anthropogenic activities,
the smoothing of actual extreme values in the simulation and the ignorance of the line of the sun sight for the simulation. The
variations of the XCH_4 at the five different sampling sites on the same day are similar (Fig.9), but the measurements show
375   more extreme values (e.g., 4th July), compared to the simulations. A further analysis in a future study is suggested to provide
deeper insight on site-specific transport characteristics.

As a final point in our analysis, we focus on simulated $\Delta\overline{XCO_2}$ values for these four target dates (Fig.10). The $\Delta\overline{XCO_2}$ (blue line) on 3rd, 4th, 6th and 10th July in five sampling sites are mainly dominated by the XCO_2 changes caused by the anthropogenic tracer (red), instead of the VPRM tracer (green). Compared to the left column of Figure.8, the red line and blue line in Fig.10 show a stronger similarity in their trends. With this form of DCM (compared to the original form Eq.5 in Sect.4.1), anthropogenic activities can be clearly shown to influence XCO_2 within urban areas. Meanwhile, the ΔXCO_2 measurements (black) fit better with the simulation with a RMSE of $0.2333\,\mathrm{ppm}$, compared to the comparisons of ΔXCO_2 depicted in the left column of Fig.7 (RMSE=$0.2973\,\mathrm{ppm}$).

5 Discussion and conclusion

We used WRF-GHG to quantitatively simulate the uptake, emission and transport of CO_2 and CH_4 for Berlin with a high resolution of 1 km. The simulated wind and concentration fields were compared with observations from 2014. Then, differential column methodology (DCM) was utilized as a post-processing method for the XCH_4 comparison and the XCO_2 tracer analysis.

The measured and simulated wind fields at 10 meters mostly demonstrate good agreement but with slight errors in the wind directions. The simulated pressure vertical profile and the averaging kernel from the solar-viewing spectrometer (EM27/SUN) are used to obtain the smoothed pressure-weighted average concentration for further comparisons. The simulated XCO_2 concentrations actually reproduce the observations well, but with approx. 1-2 ppm bias which can attribute to the coarse emission inventory, background concentrations from CAMS and the ignorance of the line of the sun sight for the simulation. Compared with the measured XCH_4, some deviations can clearly be noted in the the simulated XCH_4, caused by the relatively high initialization of background concentration fields and the errors in the tropopause height potentially. We discussed the diurnal variation of concentration components corresponding to the major emission tracers for both CO_2 and CH_4. The biogenic component plays a pivotal role in the variations of XCO_2. The impact from anthropogenic emission sources is somewhat weak compared to this, while the XCH_4 enhancement is dominated by human activities.

We then concentrated on using DCM for focusing our analysis on relevant CO_2 and CH_4 contributions from the urban area. DCM highlights that the enhancement of XCO2 over background within the inner Berlin urban area is mostly caused by anthropogenic activities. In DCM, wind direction plays a vital role to define the upwind and downwind sites, which directly influence the calculation of differential column concentrations. In the CO_2 tracer analysis, it turns out that $\Delta\overline{XCO_2}$, the difference with respect to a mean value instead of a specific upwind site, exhibits a more visible and clearer trend, which proves that the CO_2 enhancement is dominated by anthropogenic activities within the urban area. We conclude that DCM, when applied with care, helps to highlight the relevant emission sources. Similarly, for XCH_4, DCM eliminates the bias of the simulated values. Furthermore, when ΔXCH_4 values suffer from inconsistent wind directions, we consider $\Delta\overline{XCH_4}$ to be a useful quantity for analysis.

An analysis of XCO_2 in the Paris hot-spot region was carried out by Vogel et al. (2019). Some of their results can be compared to the conclusions we drew in this paper. In Vogel et al. (2019), the modelled XCO_2 was calculated based on the chemistry transport model CHIMERE (2 km) and flux framework CAMS (15 km), with hourly anthropogenic emissions from the IER

and EDGAR emission inventories, and the natural fluxes prescribed by the C-Tessel model (Sect.2 in Vogel et al. (2019)). When comparing results from our simulation, the diurnal variation in the XCO_2 enhancement over background (Sect.3.4 and Fig.4(a) of our paper) is comparable to the findings of Vogel et al. (2019). For the analysis on the comparison of ΔXCH_4 between simulations and measurements in Sect.4.1, we found that negative column concentration differences between down- and upwind sites appear for some periods, owing to the variation of wind directions that causes the conversion of up- and downwind sites, which was also mentioned for the ΔXCO_2 analysis in Vogel et al. (2019). Based on the CHIMERE-CAMS modelling framework, they showed that the strong decrease in XCO_2 during daytime can be linked to net ecosystem exchange, while a significant enhancement compared to the background is caused by XCO_2 from fossil fuel emissions, but this is often compensated by net ecosystem exchange. We utilized DCM to bring out the role of anthropogenic activities within urban areas (see the XCO_2 tracer analysis in Sect.4 of our paper).

We conclude that WRF-GHG is a suitable model for precise GHG transport analysis in urban areas, especially when combined with DCM. DCM is not only useful for the direct evaluation of measurements, but also helps us to understand the results of tracer transport models, canceling out the bias caused, e.g., by initialization conditions, and highlighting regional emission sources. This case is a fundamental study for the WRF-GHG mesoscale modelling framework which is being built to combined with the first worldwide permanent fully-automated column network for GHGs and NOx in Munich.

In future work, we suggest running WRF-GHG for more urban areas, such that, e.g., different transport, more emission tracers, topography, emission scenarios and the quantification of model errors can be studied. The influence from the line of the sun sight should be taken into account and the relative sensitivity analysis is suggested. The WRF-GHG mesoscale simulation framework may also be combined with microscale atmospheric transport models to simulate crucial details of emission sources and transport patterns precisely, with the aim of tracing urban GHG emissions. A further promising direction for future studies may be the application of DCM and model-based analysis to satellite measurements, to assess gradients across column concentrations with a dense spatial sampling.
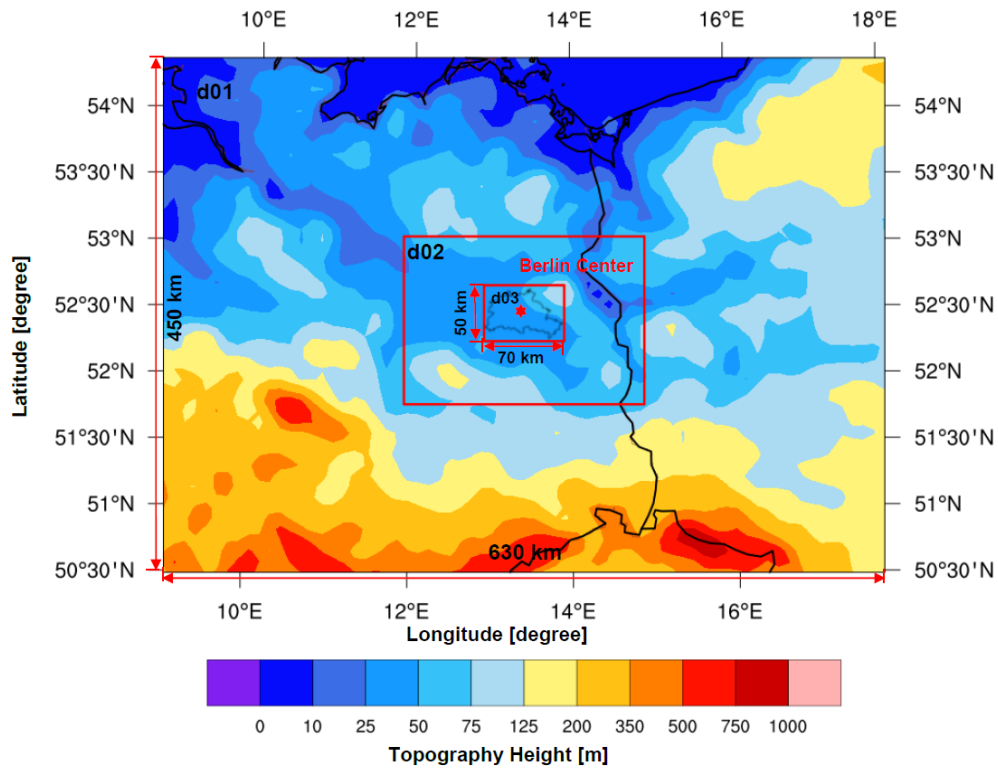
Data availability.

The simulation data that support the findings of this study are available on request from the corresponding author. The measurement data are available at doi:10.5194/amt-8-3059-2015 (Hase et al., 2015).
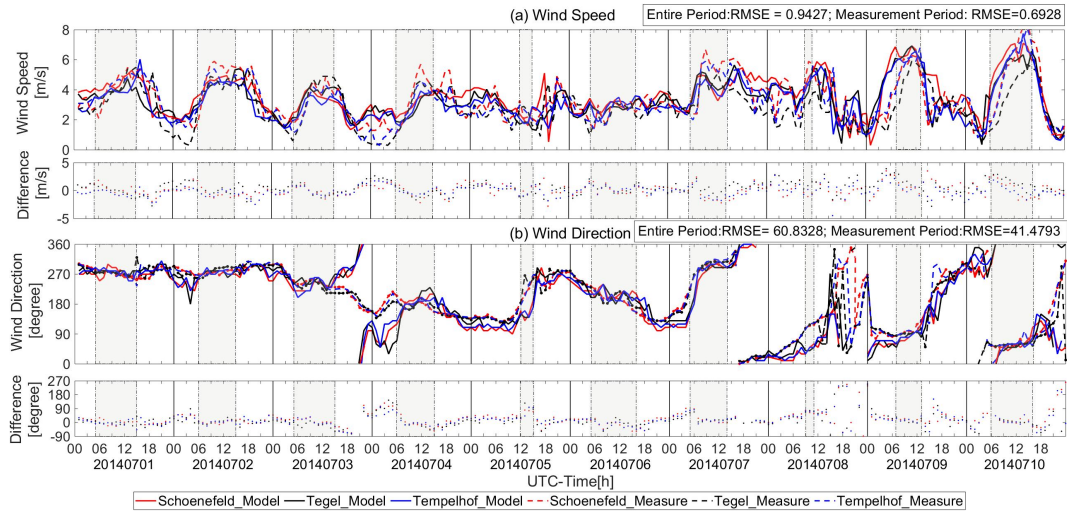
Competing interests.

The authors declare that they have no conflict of interest.

Figure 1. The topography map for the three domains in our study. The domain d03 is centered over Berlin, at 13.383°N, 52.517°E, marked with a red star. The boundary of Berlin from GADM (available at https://gadm.org/) is depicted in the innermost domain.

Figure 2. Variation and differences between simulated and measured wind fields for (a) wind speeds and (b) wind directions from 1st to 10th July 2014 at the three measurement sites, Schönefeld (red lines), Tegel (black) and Tempelhof (blue) in Berlin. The solid lines represent the simulated wind fields provided by WRF-GHG and the dashed lines depict the measured wind fields. The differences in (a)&(b) are simulations minus measurements. FTS measurement time periods on each date are marked by gray shaded areas.
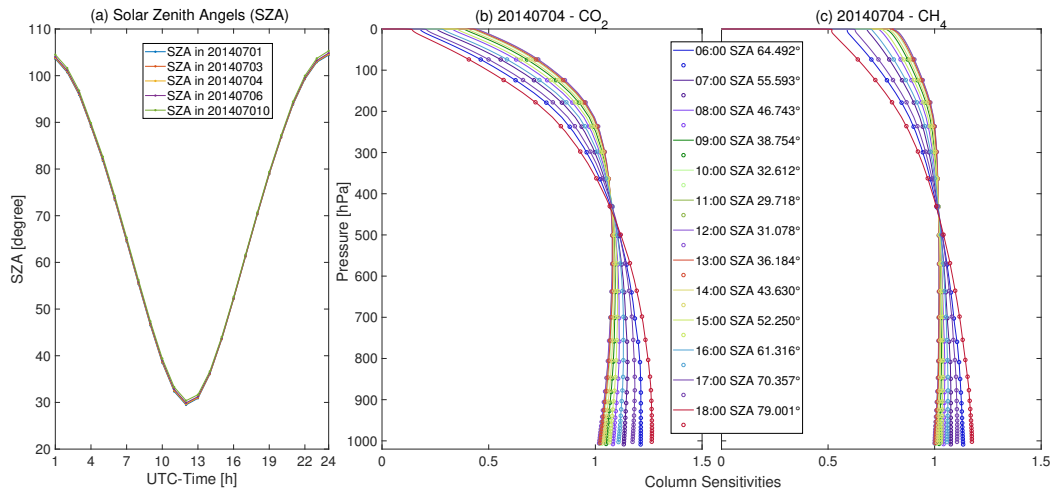

Figure 3. (a) Daily variations of solar zenith angle (SZA) for five simulation dates (1st, 3rd, 4th, 6th and 10th July) and the vertical distributions of column sensitivities for (b) CO_2 and (c) CH_4 on 4th July. (b) & (c): the solid lines represent our derived column sensitivities for EM27/SUN under different SZAs, and the circles stand for the values on model pressure levels.
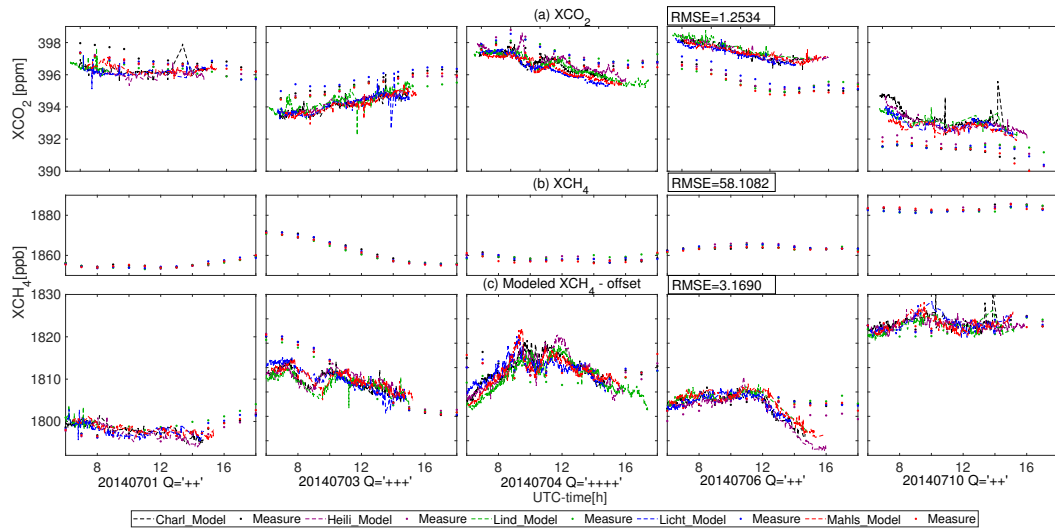
Figure 4. Variations of the measured and smoothed simulated (a) XCO_2 and (b) XCH_4 on 1st, 3rd, 4th, 6th and 10th July 2014, for five sampling sites in Berlin: Charlottenburg (Charl: black markers), Heiligensee (Heili: purple), Lichtenrade (Licht: green), Lindenberg (Lind: blue) and Mahlsdorf (Mahls: red). The solid circles in (a) and (b) stand for the simulated values provided by WRF-GHG and the dashed lines represent the measured concentrations. The solid circles represent the simulated XCH_4 after the subtraction of the daily offset in (c).
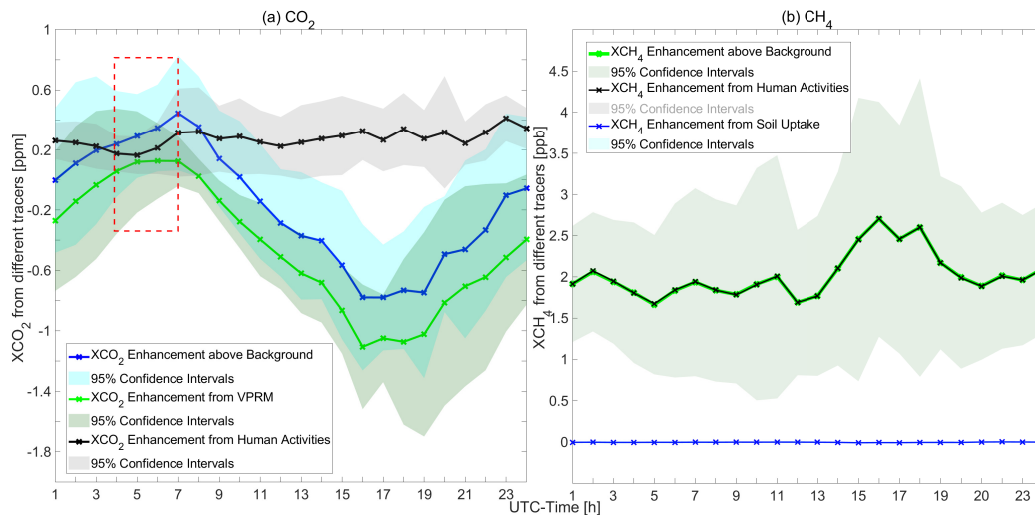

Figure 5. The diurnal variations of the simulated changes in concentrations caused by different emission tracers in Charlottenburg in Berlin from 2014, averaged over a period of nine days (from 2nd to 10th July 2014). The colored lines represent the concentration changes and the mean enhancement over background. (a): the mean hourly $XCO_{2,VPRM}$ (green line) and $XCO_{2,anthro}$ (black); (b): the mean hourly $XCH_{4,anthro}$ (black) and $XCH_{4,soil}$ (blue). The red box in (a) marks the morning peak of the XCO_2 enhancement over the background, as described in Sect.3.4.

18
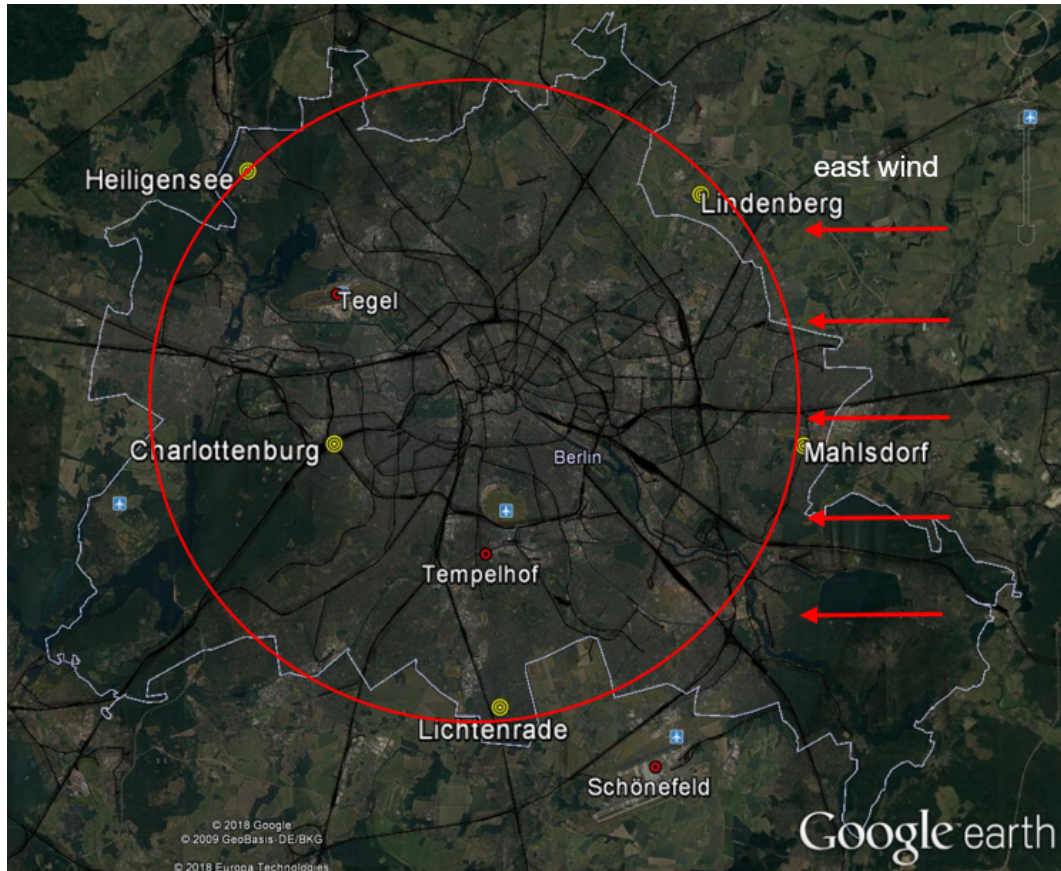
Figure 6. Detailed locations of the five sampling sites.The five red stars stand for the five sampling sites, four of which (Mahlsdorf, Heiligensee, Lindenberg and Lichtenrade) were roughly situated along a circle with a radius of 12 km around the center of Berlin, marked as the black circle. The innermost domain of our WRF-GHG model contains all five measurement sites. The three wind measurement sites are marked by red circles. Map provided by Google Earth.
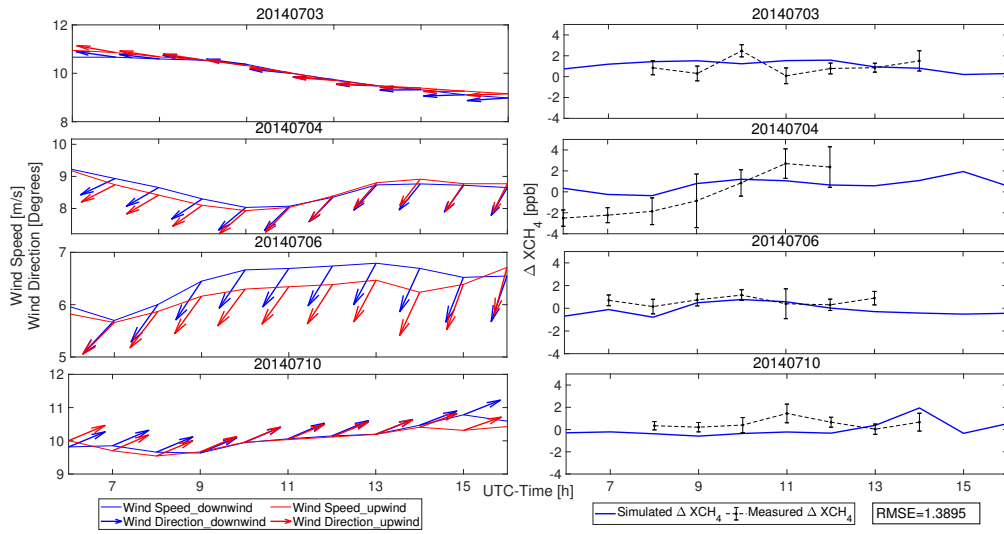
Figure 7. Modeled wind fields for downwind (blue lines) and upwind (red) sites (left column), and downwind-minus-upwind differential evaluation for measured (blue) and simulated (black) XCH₄ (right column) on 3rd, 4th, 6th and 10th July 2014. Based on the selection of downwind and upwind sites in Table.1, ΔXCH₄ is calculated using Eq.6, 7 and 8, depicted by blue lines for measurements and black lines for simulations. The black error bars in the right column are the standard derivations of the minute values of the hourly mean.
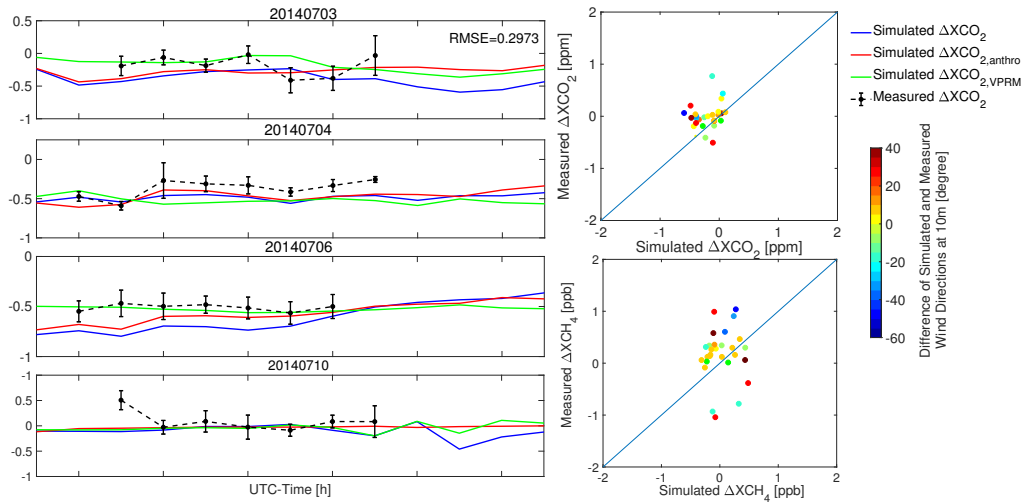
Figure 8. Measured (black lines) and simulated (blue) ΔXCO₂ on 3rd, 4th, 6th and 10th July 2014, and Comparison of hourly mean ΔXCO₂ and ΔXCH₄ for these four days. The ΔXCO₂, calculated using Eq.6, 7 and 8, are depicted by blue lines in the right column. The red and green lines show the variation of the differences between downwind and upwind sites in XCO₂ changes from anthropogenic and biogenic activities, respectively. The points color in right column are coded by the difference of the simulated and measured wind directions at 10 meters. The black error bars in the left column are the standard derivations of the minute values of the hourly mean.
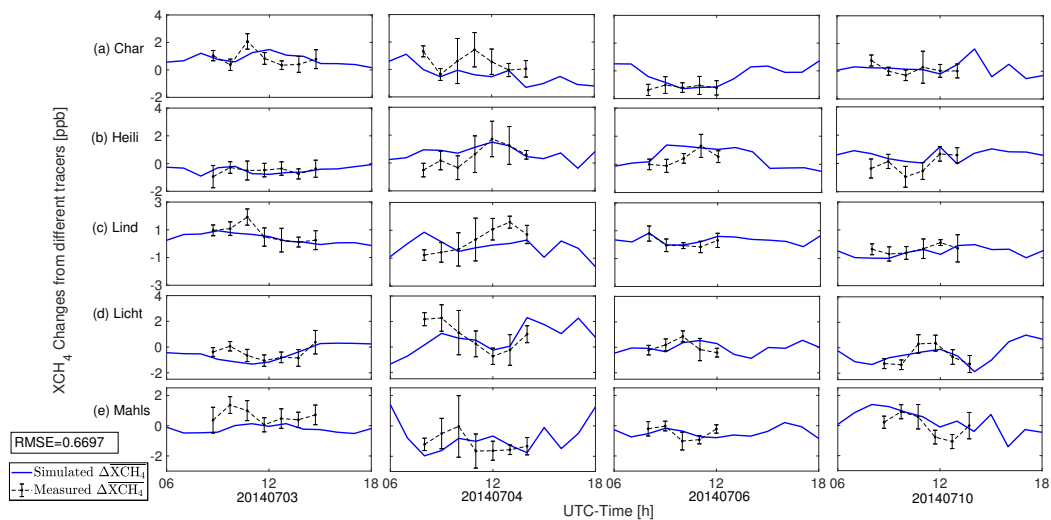
Figure 9. Modelled (blue lines) and observed (black) site XCH₄ vs. site-mean XCH₄ data for five sampling sites: Charlottenburg (Char: 1st row), Heiligensee (Heili: 2nd row), Lindenberg (Lind: 3rd row), Lichtenrade (Licht: 4th row) and Mahlsdorf (Mahls: 5th row). The black error bars in each subplot are the standard derivations of the minute values of the hourly mean.
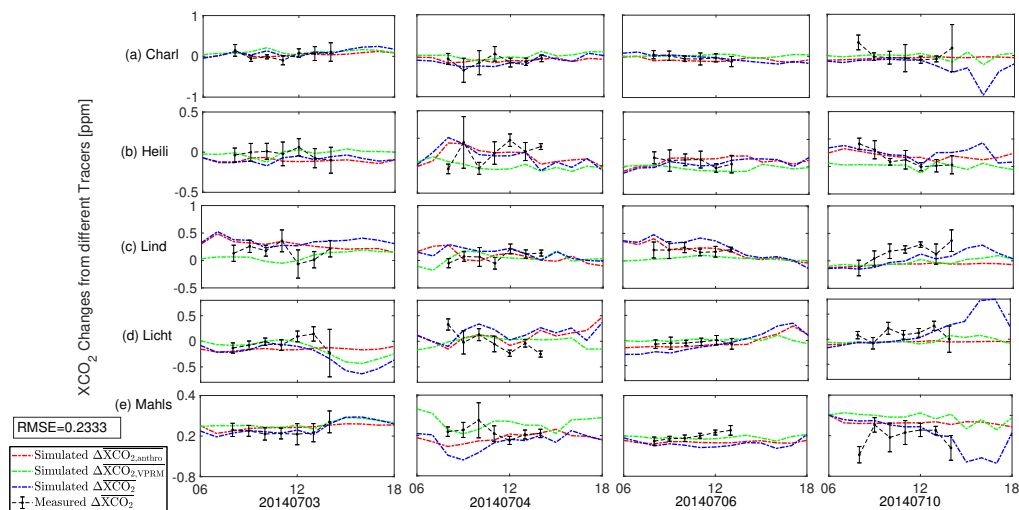
Figure 10. $\Delta\overline{XCO_2}$ (blue lines for simulations and black for measurements) for five sampling sites (i.e. the difference between XCO_2 at the site and the mean XCO_2 of five sampling sites): Charlottenburg (Char: 1st row), Heiligensee (Heili: 2nd row), Lindenberg (Lind: 3rd row), Lichtenrade (Licht: 4th row) and Mahlsdorf (Mahls: 5th row). We furthermore show the differences in the simulated XCO_2 changes from biogenic (green) and anthropogenic (red) activities. The black error bars in each subplot are the standard derivations of the minute values of the hourly mean.

Table 1. The selections of upwind and downwind sites for four dates

Date	Wind Direction (degree)	Upwind Sites	Downwind Sites
3rd Jul:	272.55 ±20.19	Charlottenburg/Lichtenrade	Lindenberg/Mahlsdorf
4th Jul:	206.93 ±24.23	Lichtenrade	Heiligensee/Lindenberg
6th Jul:	214.51 ±26.38	Lichtenrade	Heiligensee/Lindenberg
10th Jul:	38.03 ±25.33	Mahlsdorf/Lindenberg	Lichtenrade/Charlottenburg

Wind directions are the mean of the hourly vertical-mean wind directions for one day.

Appendix A: WRF-GHG running process

A detailed description on how to run WRF-GHG is provided in Beck et al. (2011), and thus, only the initialization process for our study in particular is summarized here. One daily simulation with WRF-GHG is normally performed for a 30-hour time period including a 6-hour spin up for the meteorology from 18 UTC to 24 UTC of the previous day and a 24-hour simulation of the tracer transport on the actual simulation day (Beck et al., 2011).

As for the boundary conditions, a small constant offset needs to be added into the WRF boundary files for the biospheric CO_2 and the soil sink CH_4 tracers at the start of each run, because these tracers can result in a net sink. When the concentrations become negative, the advected tracer fields will "disappear", as the WRF code does not allow tracers with negative values. An offset applied in the initialization process helps to avoid this problem and later is subtracted in the post-processing. As for the initial conditions, the meteorological conditions are initialized with external data sources (GFS in our model) each day to update the WRF meteorological fields properly. The tracers for the total and background CO_2 and CH_4 flux fields are initialized only once, at the first day of the simulation period, using CAMS as an external data source. Furthermore, the lateral boundary conditions of the outer domain d01 is also initialized by the CAMS. Then, for the other days within the simulation period, these tracers for the total and background CO_2 and CH_4 fluxes are directly taken from the final WRF output at 24 UTC of the previous day to make the entire simulation continuous. The CO_2 tracer for VPRM and the CH_4 tracer for soil uptake are also initialized with a constant offset to avoid the appearance of negative values caused, e.g., by the vegetation respiration (Beck et al., 2011). In terms of the other flux tracers, the tracer variables are initialized each day, using external data sources to provide the updated emission data for each tracer.

Appendix B: Model systematic equation errors for Eq.1

In the passive tracer transport simulation, the total concentration of each GHG is represented as a separate tracer, giving redundant information (with respect to the sum of all tracers for each GHG), allowing for consistency checks. A variety of flux models and emission inventories implemented in the modules of WRF-GHG are used for the estimation of GHG fluxes. The flux values from external emission inventories are gridded and ingested into the model. In the transport process, the relationship among the changes in concentrations from different emission tracers, the total and background concentrations (Eq.1) should then be satisfied; ideally with ΔCO_2 and ΔCH_4 computational errors during the simulation process being zero. Nonzero values of ΔCO_2 and ΔCH_4 reflect the limited precision of the tracer transport calculation in WRF-GHG.

Figure.B1 thus shows the mean values (solid lines) and the 95 % confidence intervals of ΔCO_2 and ΔCH_4. As depicted in the figure, ΔCO_2 ranges from -0.005 ppm to 0.01 ppm while ΔCH_4 is in range of -0.01 ppb to 0.02 ppb. Divided by typical absolute values of the concentrations from different flux processes for XCO_2 (around 1 ppm) and XCH_4 (around 2-3 ppb) depicted in Fig.4, the relative computational error is found to be ~1 % for both CO_2 and CH_4.

These tiny computational errors can be caused by the slight non-linearity of the advection scheme used in the WRF-GHG model, which makes the sum of the concentrations in CO_2 and CH_4 from all individual flux tracers not exactly equal to the concentration from the "sum tracer", representing the total sum of all fluxes related to different processes.
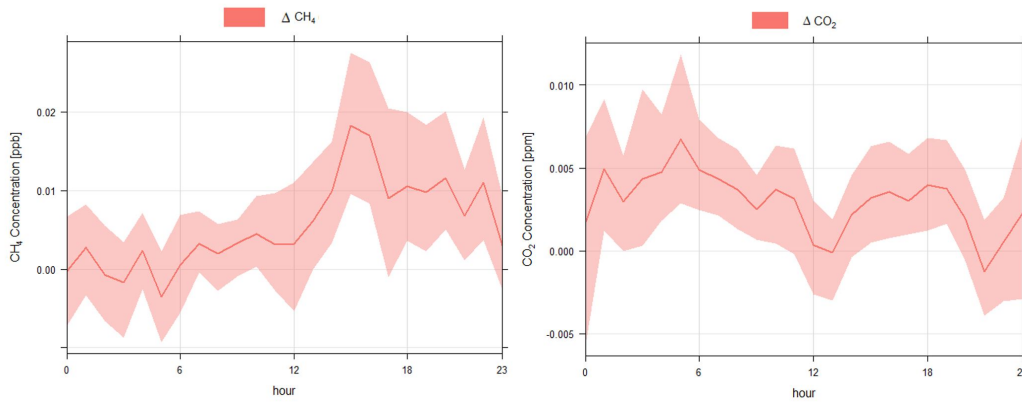
Figure B1. The mean values (solid lines) and the 95 % confidence intervals of the computational error ΔCO_2 (left) and ΔCH_4 (right). ΔCO_2 and ΔCH_4 are calculated using Eq.1.

485 **Appendix C: The vertical distribution of CH_4 in CAMS**
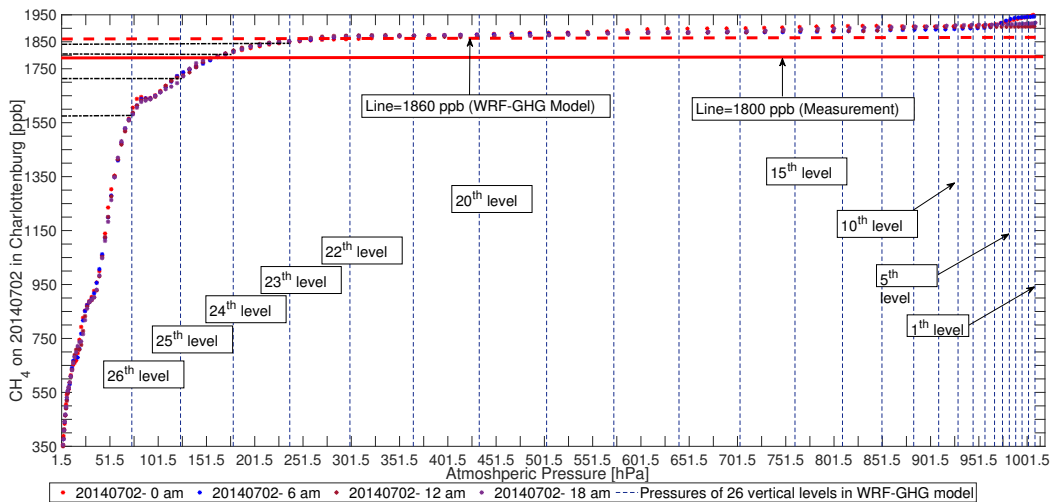
Figure C1. The vertical distribution of CH_4 on 2nd July in Charlottenburg. The asterisks represent the XCH_4 field from CAMS. The vertical dashed lines show the values of atmospheric pressure corresponding to the 26 vertical levels in our WRF-GHG. Y-axis levels of 1800 ppb and 1860 ppb, corresponding to the total column measurement and the modeled value, respectively, have been marked by red horizontal (solid / dashed) lines.
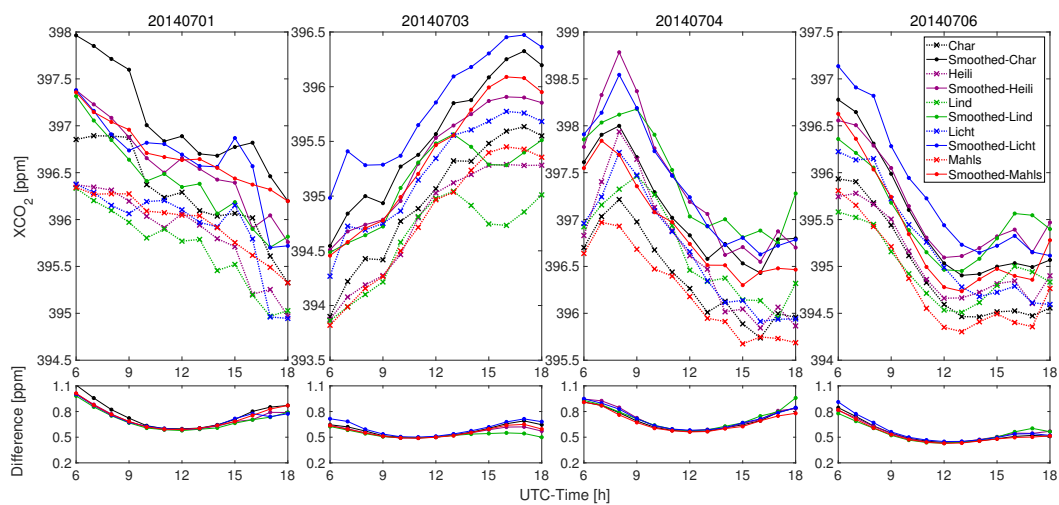
Figure D1. Comparison of XCO$_2$ from WRF-GHG with and without smoothing (using our column sensitivities for EM27/SUN) for the first four simulated dates. The five colors stand for the concentrations from five sample sites. Dotted lines with the makers 'x' represent the XCO$_2$ without smoothing, while solid lines with the markers 'o' stand for the smoothed values.
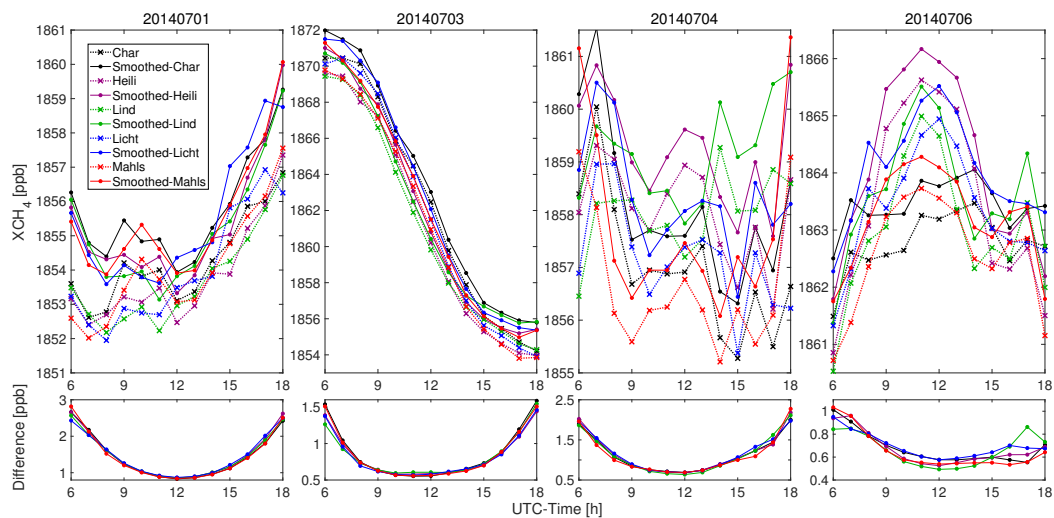
Figure D2. Comparison of XCH$_4$ from WRF-GHG with and without smoothing (using our column sensitivities for EM27/SUN) for the first four simulated dates. The five colors stand for the concentrations from five sample sites. Dotted lines with the makers 'x' represent the XCH$_4$ without smoothing, while solid lines with the markers 'o' stand for the smoothed values.

Appendix D: Accounting for instrumental limitations in comparison of measured to simulated XCO$_2$ and XCH$_4$

Appendix E: The vertical wind profiles for wind speeds and wind directions
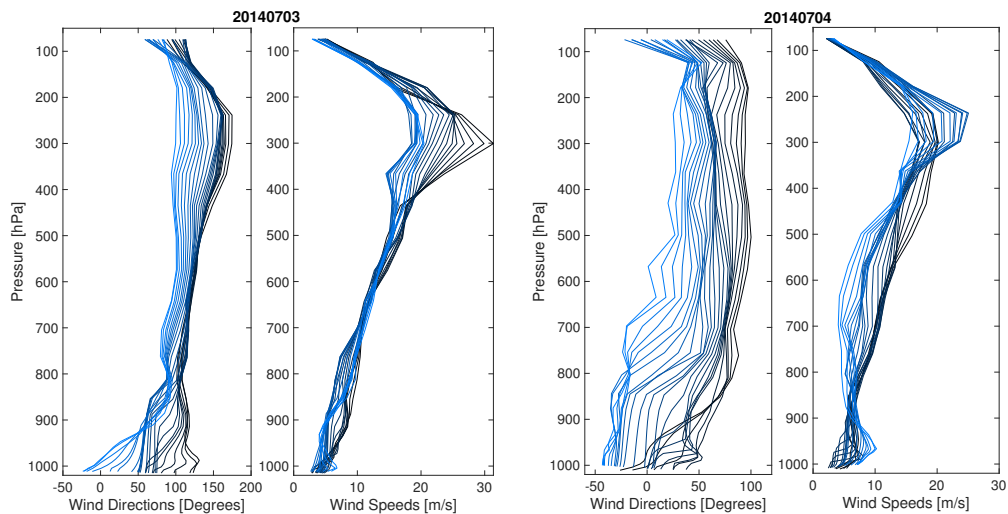
Figure E1. The vertical distribution of wind fields (wind speeds and wind directions) on 3rd July (left side) and 4th July (right side) in Tegel. The colors from black to blue represent the time from morning to evening.

References

Agusti-Panareda, A., Diamantakis, M., Bayona, V., Klappenbach, F., and Butz, A.: Improving the inter-hemispheric gradient of total column atmospheric CO_2 and CH_4 in simulations with the ECMWF semi-Lagrangian atmospheric global model, Geoscientific Model Development, 10, 1–18, https://doi.org/10.5194/gmd-10-1-2017, 2017.

Ahmadov, R., Gerbig, C., Kretschmer, R., Koerner, S., Neininger, B., Dolman, A., and Sarrat, C.: Mesoscale covariance of transport and CO_2 fluxes: Evidence from observations and simulations using the WRF-VPRM coupled atmosphere-biosphere model, Journal of Geophysical Research: Atmospheres, 112, https://doi.org/10.1029/2007JD008552, 2007.

Ahmadov, R., Gerbig, C., Kretschmer, R., Körner, S., Rödenbeck, C., Bousquet, P., and Ramonet, M.: Comparing high resolution WRF-VPRM simulations and two global CO_2 transport models with coastal tower measurements of CO_2, Biogeosciences, 6, 807–817, https://doi.org/10.5194/bg-6-807-2009, 2009.

Andres, R. J., Boden, T. A., Bréon, F.-M., Ciais, P., Davis, S., Erickson, D., Gregg, J. S., Jacobson, A., Marland, G., Miller, J., et al.: A synthesis of carbon dioxide emissions from fossil-fuel combustion, Biogeosciences, 9, 1845–1871, https://doi.org/10.5194/bg-9-1845-2012, 2012.

Basart, S., Bendictow, A., Blechschmidt, A.-M., Chabrillat, S., Clark, H., Cuevas, E., Flentje, H., Hansen, K. M., Kapsomenakis, U. Im, J., Langerock, B., Petersen, K., Richter, A., Sudarchikova, N., Thouret, V., Warneke, T., and Zerefos, C.: Validation report of the CAMS near-real time global atmospheric composition service, 2017.

Beck, V., Koch, T., Kretschmer, R., Marshall, J.and Ahmadov, R., Gerbig, C., Pillai, D., and Heimann, M.: The WRF Greenhouse Gas Model (WRF-GHG). Technical Report No. 25, Max Planck Institute for Biogeochemistry, Jena, Germany., 2011.

Bergamaschi, P., Corazza, M., Karstens, U., Athanassiadou, M., Thompson, R. L., Pison, I., Manning, A., Bousquet, P., Segers, A., Vermeulen, A., et al.: Top-down estimates of European CH_4 and N_2O emissions based on four different inverse models, Atmospheric Chemistry and Physics, 15, 715–736, https://doi.org/10.5194/acp-15-715-2015, 2015.

Bergamaschi, P., Karstens, U., Manning, A. J., Saunois, M., Tsuruta, A., Berchet, A., Vermeulen, A. T., Arnold, T., Janssens-Maenhout, G., Hammer, S., et al.: Inverse modelling of European CH_4 emissions during 2006–2012 using different inverse models and reassessed atmospheric observations, Atmospheric Chemistry and Physics, 18, 901–920, https://doi.org/10.5194/acp-18-901-2018, 2018.

Caulton, D. R., Shepson, P. B., Santoro, R. L., Sparks, J. P., Howarth, R. W., Ingraffea, A. R., Cambaliza, M. O., Sweeney, C., Karion, A., Davis, K. J., et al.: Toward a better understanding and quantification of methane emissions from shale gas development, Proceedings of the National Academy of Sciences, p. 201316546, https://doi.org/10.1073/pnas.1316546111, 2014.

Chen, F., Kusaka, H., Bornstein, R., Ching, J., Grimmond, C., Grossman-Clarke, S., Loridan, T., Manning, K. W., Martilli, A., Miao, S., et al.: The integrated WRF/urban modelling system: development, evaluation, and applications to urban environmental problems, International Journal of Climatology, 31, 273–288, https://doi.org/10.1002/joc.2158, 2011.

Chen, J., Samra, J., Gottlieb, E., Budney, J., Wofsy, S. C., McKain, K., Hase, F., Gerbig, C., Chance, K., and McManus, J.: Novel instrumentation for column measurements and regional eulerian modeling for network design in Boston, in: AGU Fall Meeting Abstracts, 2013.

Chen, J., Viatte, C., Hedelius, J. K., Jones, T., Franklin, J. E., Parker, H., Gottlieb, E. W., Wennberg, P. O., Dubey, M. K., and Wofsy, S. C.: Differential column measurements using compact solar-tracking spectrometers, Atmospheric Chemistry and Physics, 16, 8479–8498, https://doi.org/10.5194/acp-16-8479-2016, 2016.

Chen, J., Dietrich, F., Franklin, J. E., Jones, T. S., André, B., Luther, A., Kleinschek, R., Hase, F., Wenig, M., Ye, S., Nouri, A., Frey, M., Knote, C., Alberti, C., and Wofsy, S.: Mesoscale column network for assessing GHG and NOx emissions in Munich, EGU General Assembly Conference Abstracts, Vol.20, EGU2018-10192-2, Vienna, Austria, 8–13 April 2018, https://meetingorganizer.copernicus.org/EGU2018/EGU2018-10192-2.pdf, 2018.

Cressot, C., Chevallier, F., Bousquet, P., Crevoisier, C., Dlugokencky, E., Fortems-Cheiney, A., Frankenberg, C., Parker, R., Pison, I., Scheepmaker, R., et al.: On the consistency between global and regional methane emissions inferred from SCIAMACHY, TANSO-FTS, IASI and surface measurements, Atmospheric Chemistry and Physics, 14, 577–592, https://doi.org/10.5194/acp-14-577-2014, 2014.

Deutscher, N. M., Notholt, J., Messerschmidt, J., Weinzierl, C., Warneke, T., Petri, C., Grupe, P., and Katrynski, K.: TCCON data from Bialystok (PL), Release GGG2014R1, TCCON data archive, hosted by CaltechDATA, https://doi.org/10.14291/tccon.ggg2014.bialystok01.R1/1183984, https://tccondata.org, 2014.

Fragkias, M., Lobo, J., Strumsky, D., and Seto, K. C.: Does size matter? Scaling of CO_2 emissions and US urban areas, PLoS One, 8, e64 727, https://doi.org/10.1371/journal.pone.0064727, 2013.

Franklin, J. E., Jones, T. S., Chen, J., Parker, H., Hedelius, J., Wennberg, P., Dubey, M. K., Cohen, Ron C., G. A., Sargent, M., Davis, K. J., Mielke, L., Fischer, M., and Wofsy, S.: A three-dimensional observation network for determining urban emissions of CO_2 and CH_4, 2017 North American Carbon Program, North Bethesda, MD, USA, https://www.nacarbon.org/meeting_2017/abs_and_discussions/mtg2017_ab_searchab_id161.html, 2017.

Fraunhofer-Gesellschaft: ISE: Map of Power Plants| Energy Chart, data source: European Energy Exchange (EEX), https://www.energy-charts.de/osm.htm, assessed August 14th, 2018, 2018.

Frey, M., Hase, F., Blumenstock, T., Groß, J., Kiel, M., Mengistu Tsidu, G., Schäfer, K., Sha, M., and Orphal, J.: Calibration and instrumental line shape characterization of a set of portable FTIR spectrometers for detecting greenhouse gas emissions, Atmospheric Measurement Techniques, 8, 3047–3057, https://doi.org/10.5194/amt-8-3047-2015, 2015.

Friedl, M. A., Sulla-Menashe, D., Tan, B., Schneider, A., Ramankutty, N., Sibley, A., and Huang, X.: MODIS collection 5 global land cover: Algorithm refinements and characterization of new datasets, 2001-2012, Collection 5.1 IGBP Land Cover, Boston University, Boston, MA, USA, 2010.

Galkowski, M., Gerbig, C., Marshall, J., Koch, F., Chen, J., Baum, S., Jordan, M., Fiehn, A., Roiger, A., Jöckel, P., Nickl, A., Mertens, M., Bovensmann, H., Necki, J., Swolkien, J., Ehret, G., Kiemle, C., Amediek, A., Quatrevalet, M., and Fix, A.: Airborne in-situ measurements of CO_2 and CH_4 and their interpretation using WRF-GHG: results from the HALO CoMet 1.0 campaign, EGU General Assembly Conference Abstracts, Vol. 21, EGU2019-14091, Vienna, Austria, 8–13 April 2019, https://meetingorganizer.copernicus.org/EGU2019/EGU2019-14091.pdf, 2019.

Gerbig, C., Körner, S., and Lin, J.: Vertical mixing in atmospheric tracer transport models: error characterization and propagation, Atmospheric Chemistry and Physics, 8, 591–602, https://doi.org/10.5194/acp-8-591-2008, 2008.

Gisi, M., Hase, F., Dohe, S., Blumenstock, T., Simon, A., and Keens, A.: XCO_2-measurements with a tabletop FTS using solar absorption spectroscopy, Atmospheric Measurement Techniques, 5, 2969–2980, https://doi.org/10.5194/amt-5-2969-2012, 2012.

Hardiman, B. S., Wang, J. A., Hutyra, L. R., Gately, C. K., Getson, J. M., and Friedl, M. A.: Accounting for urban biogenic fluxes in regional carbon budgets, Science of the Total Environment, 592, 366–372, https://doi.org/10.1016/j.scitotenv.2017.03.028, 2017.

Hase, F., Frey, M., Blumenstock, T., Groß, J., Kiel, M., Kohlhepp, R., Mengistu Tsidu, G., Schäfer, K., Sha, M., and Orphal, J.: Application of portable FTIR spectrometers for detecting greenhouse gas emissions of the major city Berlin, Atmospheric Measurement Techniques, 8, 3059–3068, https://doi.org/10.5194/amt-8-3059-2015, 2015.

Hedelius, J. K., Viatte, C., Wunch, D., Roehl, C. M., Toon, G. C., Chen, J., Jones, T., Wofsy, S. C., Franklin, J. E., Parker, H., et al.: Assessment of errors and biases in retrievals of XCO_2, XCH_4, XCO, and XN_2O from a 0.5 cm–1 resolution solar-viewing spectrometer, Atmospheric Measurement Techniques, 9, 3527–3546, https://doi.org/10.5194/amt-9-3527-2016, 2016.

565 Holmes, C. D.: Methane Feedback on Atmospheric Chemistry: Methods, Models, and Mechanisms, Journal of Advances in Modeling Earth Systems, 10, 1087–1099, https://doi.org/10.1002/2017MS001196, 2018.

Homann, G.: Climate Protection in Berlin, Tech. rep., Senate Department for the Environment, Transport and Climate Protection, https://www.berlin.de/senuvk/klimaschutz/politik/download/klimaschutzpolitik_en.pdf, 2018.

Hopkins, F. M., Ehleringer, J. R., Bush, S. E., Duren, R. M., Miller, C. E., Lai, C.-T., Hsu, Y.-K., Carranza, V., and Randerson, J. T.: Mitigation

570 of methane emissions in cities: How new measurements and partnerships can contribute to emissions reduction strategies, Earth's Future, 4, 408–425, https://doi.org/10.1002/2016EF000381, 2016.

IEA: (International Energy Agency).: World Energy Outlook 2008, https://www.iea.org/media/weowebsite/2008-1994/WEO2008.pdf, 2008.

IEA: International Energy Agency :Cities, Towns & Renewable Energy, Tech. rep., http://www.iea.org/publications/freepublications/publication/cities2009.pdf, 2009.

575 IPCC: (International Panel on Climate Change).: IPCC fifth assessment report: Climate change 2014 Synthesis Report. Summary for Policy-makers, http://www.ipcc.ch/pdf/assessment-report/ar5/syr/AR5_SYR_FINAL_SPM.pdf, 2014.

Janssens-Maenhout, G., Crippa, M., Guizzardi, D., Dentener, F., Muntean, M., Pouliot, G., Keating, T., Zhang, Q., Kurokawa, J., Wankmüller, R., et al.: HTAP_v2: a mosaic of regional and global emission gridmaps for 2008 and 2010 to study hemispheric transport of air pollution., Atmospheric Chemistry and Physics, 15, 11 411–11 432, https://doi.org/10.5194/acp-15-11411-2015, 2015.

580 Kennedy, C., Steinberger, J., Gasson, B., Hansen, Y., Hillman, T., Havranek, M., Pataki, D., Phdungsilp, A., Ramaswami, A., and Mendez, G. V.: Greenhouse gas emissions from global cities, 43, 7297–7302, https://doi.org/10.1021/es900213p, 2009.

Kindler, A., Klimeczek, H.-J., and Franck, U.: Socio-spatial distribution of airborne outdoor exposures–An indicator for environmental quality, quality of life, and environmental justice: The case study of Berlin, in: Urban Transformations, pp. 257–279, Springer, https://doi.org/10.1007/978-3-319-59324-1_14, 2018.

585 Kivi, R. and Heikkinen, P.: Fourier transform spectrometer measurements of column CO_2 at Sodankylä, Finland, Geoscientific Instrumentation, Methods and Data Systems, 5, 271–279, https://doi.org/10.5194/gi-5-271-2016, 2016.

Kretschmer, R., Gerbig, C., Karstens, U., and Koch, F.-T.: Error characterization of CO_2 vertical mixing in the atmospheric transport model WRF-VPRM, Atmospheric Chemistry and Physics, 12, 2441–2458, https://doi.org/10.5194/acp-12-2441-2012, 2012.

Mahadevan, P., Wofsy, S. C., Matross, D. M., Xiao, X., Dunn, A. L., Lin, J. C., Gerbig, C., Munger, J. W., Chow, V. Y., and Gottlieb, E. W.: A

590 satellite-based biosphere parameterization for net ecosystem CO_2 exchange: Vegetation Photosynthesis and Respiration Model (VPRM), Global Biogeochemical Cycles, 22, https://doi.org/10.1029/2006GB002735, 2008.

Marcotullio, P. J., Sarzynski, A., Albrecht, J., Schulz, N., and Garcia, J.: The geography of global urban greenhouse gas emissions: An exploratory analysis, Climatic Change, 121, 621–634, https://doi.org/10.1007/s10584-013-0977-z, 2013.

McKain, K., Wofsy, S. C., Nehrkorn, T., Eluszkiewicz, J., Ehleringer, J. R., and Stephens, B. B.: Assessment of ground-based atmospheric

595 observations for verification of greenhouse gas emissions from an urban region, Proceedings of the National Academy of Sciences, 109, 8423–8428, https://doi.org/10.1073/pnas.1116645109, 2012.

Montzka, S. A., Dlugokencky, E. J., and Butler, J. H.: Non-CO_2 greenhouse gases and climate change, Nature, 476, 43–50, https://doi.org/10.1038/nature10322, 2011.

Muntean, M., Janssens-Maenhout, G., Song, S., Selin, N. E., Olivier, J. G., Guizzardi, D., Maas, R., and Dentener, F.: Trend analysis from 1970 to 2008 and model evaluation of EDGAR.V4 global gridded anthropogenic mercury emissions, Science of the Total Environment, 494, 337–350, https://doi.org/10.1016/j.scitotenv.2014.06.014, 2014.

Newman, S.and Xu, X., Gurney, K. R., Hsu, Y. K., Li, K. F., Jiang, X., Keeling, R., Feng, S., O'Keefe, D., Patarasuk, R., Wong, K. W., Rao, P., Fischer, M. L., and Yung, Y. L.: Toward consistency between trends in bottom-up CO_2 emissions and top-down atmospheric measurements in the Los Angeles megacity, Atmospheric Chemistry and Physics, 16, 3843–3863, https://doi.org/10.5194/acp-16-3843-2016, 2016.

Notholt, J., Petri, C., Warneke, T., Deutscher, N. M., Buschmann, M., Weinzierl, C., Macatangay, R., and Grupe, P.: TCCON data from Bremen (DE), Release GGG2014R0, TCCON data archive, hosted by CaltechDATA, https://doi.org/10.14291/tccon.ggg2014.bremen01.R0/1149275, https://tccondata.org, 2014.

Ohyama, H., Morino, I., Nagahama, T., Machida, T., Suto, H., Oguma, H., Sawa, Y., Matsueda, H., Sugimoto, N., Nakane, H., and Nakagawa, K.: Column-averaged volume mixing ratio of CO_2 measured with ground-based Fourier transform spectrometer at Tsukuba, Journal of Geophysical Research: Atmospheres, 114, https://doi.org/10.1029/2008JD011465, 2009.

Olsen, S. C. and Randerson, J. T.: Differences between surface and column atmospheric CO_2 and implications for carbon cycle research, Journal of Geophysical Research: Atmospheres, 109, https://doi.org/10.1029/2003JD003968, 2004.

Ostler, A., Sussmann, R., Patra, P. K., Houweling, S., De Bruine, M., Stiller, G. P., Haenel, F., Plieninger, J., Bousquet, P. J., Yin, Y., Saunois, M., Walker, K. A., Deutscher, N. M., Griffith, D. W. T., Blumenstock, T., Hase, F., Warneke, T., Wang, Z., Kivi, R., and Robinson, J.: Evaluation of column-averaged methane in models and TCCON with a focus on the stratosphere, Atmospheric Measurement Techniques, 9, 4843–4859, https://doi.org/10.5194/amt-9-4843-2016, 2016.

Parshall, L., Gurney, K., Hammer, S. A., Mendoza, D., Zhou, Y., and Geethakumar, S.: Modeling energy consumption and CO_2 emissions at the urban scale: Methodological challenges and insights from the United States, Energy Policy, 38, 4765–4782, https://doi.org/10.1016/j.enpol.2009.07.006, 2010.

Pillai, D., Gerbig, C., Ahmadov, R., Rödenbeck, C., Kretschmer, R., Koch, T., Thompson, R., Neininger, B., and Lavrié, J.: High-resolution simulations of atmospheric CO_2 over complex terrain–representing the Ochsenkopf mountain tall tower, Atmospheric Chemistry and Physics, 11, 7445–7464, https://doi.org/10.5194/acp-11-7445-2011, 2011.

Pillai, D., Gerbig, C., Kretschmer, R., Beck, V., Karstens, U., Neininger, B., and Heimann, M.: Comparing lagrangian and eulerian models for CO_2 transport - a step towards Bayesian inverse modeling using WRF/STILT-VPRM, Atmospheric Chemistry and Physics, 12, 8979–8991, https://doi.org/10.5194/acp-12-8979-2012, 2012.

Pillai, D., Buchwitz, M., Gerbig, C., Koch, T., Reuter, M., Bovensmann, H., Marshall, J., and Burrows, J. P.: Tracking city CO_2 emissions from space using a high-resolution inverse modeling approach: a case study for Berlin, Germany, Atmospheric Chemistry and Physics, 16, 9591–9610, https://doi.org/10.5194/acp-16-9591-2016, 2016.

Reusswig, F.and Hirschl, B. and Lass, W.: Climate-Neutrality Berlin 2050: Results of a Feasibility Study, Tech. rep., Senate Department for Urban Development and the Environment, https://www.berlin.de/senuvk/klimaschutz/studie_klimaneutrales_berlin/download/Machbarkeitsstudie_Berlin2050_EN.pdf, 2014.

Rodgers, C. D. and Connor, B. J.: Intercomparison of remote sounding instruments, Journal of Geophysical Research: Atmospheres, 108, https://doi.org/10.1029/2002JD002299, 2003.

Saikawa, E., Kim, H., Zhong, M., Avramov, A., Zhao, Y., Janssens-Maenhout, G., Jurokawa, J., Klimont, Z., Wagner, F., Naik, V., et al.: Comparison of emissions inventories of anthropogenic air pollutants and greenhouse gases in China, Atmospheric Chemistry and Physics, 17, 6393–6421, https://doi.org/10.5194/acp-17-6393-2017, 2017.

Sembhi, H., Boesch, H., Agusti-Panareda, A., and Massart, S.: MACC-III Deliverable D_0 42.3 : $Report on the quality of CH_4 analysis and forecast fields$, 2015.

SenStadtH: Berlin Environmental Atlas: 06.01 Actual Use of Built-up Areas/ 06.02 Inventory of Green and Open Spaces/ 06.01.1 Actual Use / 06.02.1 Actual Use and Vegetation Cover (Edition 2016), http://www.stadtentwicklung.berlin.de/umwelt/umweltatlas/e_text/eke601.pdf, 2016.

640 Skamarock, William C.and Klemp, J. B., Dudhia, J., Gill, D. O., Barker, D. M., Duda, M. G., Huang, X.-Y., Wang, W., and Powers, J. G.: Description of the Advanced Research WRF Version 3, Tech. rep., National Center for Atmospheric Research, https://pdfs.semanticscholar. org/ace5/4d4d1d6c9914997ad8f4e410044fdeb95b9d.pdf, 2008.

Skamarock, W. C., Klemp, J. B., Dudhia, J., Gill, D. O., Barker, D. M., Wang, W., and Powers, J. G.: A description of the advanced research WRF Version 2, Tech. rep., National Center For Atmospheric Research Boulder Co Mesoscale and Microscale Meteorology Div, 2005.

645 Toja-Silva, F., Chen, J., Hachinger, S., and Hase, F.: CFD simulation of CO_2 dispersion from urban thermal power plant: Analysis of turbulent Schmidt number and comparison with Gaussian plume model and measurements, Journal of Wind Engineering and Industrial Aerodynamics, 169, 177–193, https://doi.org/10.1016/j.jweia.2017.07.015, 2017.

Tukiainen, S., Railo, J., Laine, M., Hakkarainen, J., Kivi, R., Heikkinen, P., Chen, H., and Tamminen, J.: Retrieval of atmospheric CH4 profiles from Fourier transform infrared data using dimension reduction and MCMC, Journal of Geophysical Research: Atmospheres, 121, 10–312, 650 https://doi.org/10.1002/2015JD024657, 2016.

UNDESA: (United Nations Department of Economic and Social Affairs).: World Urbanization Prospects: The 2014 Revision, https://esa.un. org/unpd/wup/Publications/, 2014.

UNDESA: (United Nations Department of Economic and Social Affairs).: World Urbanization Prospects: The 2018 Revision, https://esa.un. org/unpd/wup/Publications/, 2018.

655 Viatte, C., Lauvaux, T., Hedelius, J. K., Parker, H., Chen, J., Jones, T., Franklin, J. E., Deng, A. J., Gaudet, B., Verhulst, K., Duren, R., Wunch, D., Roehl, C., Dubey, M., Wofsy, S., and Wennberg, P.: Methane emissions from dairies in the Los Angeles Basin, Atmospheric Chemistry and Physics, 17, 7509–7528, https://doi.org/10.5194/acp-17-7509-2017, 2017.

Vogel, F. R., Frey, M., Staufer, J., Hase, F., G., B., Xueref-Remy, I., Chevallier, F., Ciais, P., Sha, M. K., Chelin, P., Jeseck, P., Janssen, C., Te, Y.-V., Groß, J., Blumenstock, T., Tu, Q., and Orphal, J.: XCO_2 in an emission hot-spot region: the COCCON Paris campaign 2015, Atmos. 660 Chem. Phys., https://doi.org/10.5194/acp-19-3271-2019, 2019.

Wang, H., Fu, L., Lin, X., Zhou, Y., and Chen, J.: A bottom-up methodology to estimate vehicle emissions for the Beijing urban area, Science of the total environment, 407, 1947–1953, https://doi.org/10.1016/j.scitotenv.2008.11.008, 2009.

Wu, L., Broquet, G., Ciais, P., Bellassen, V., Vogel, F., Chevallier, F., Xueref-Remy, I., and Wang, Y.: What would dense atmospheric observation networks bring to the quantification of city CO_2 emissions?, Atmospheric Chemistry and Physics, 16, 7743–7771, 665 https://doi.org/10.5194/acp-16-7743-2016, 2016.

Wunch, D., Wennberg, P., Toon, G., Keppel-Aleks, G., and Yavin, Y.: Emissions of greenhouse gases from a North American megacity, Geophysical Research Letters, 36, https://doi.org/10.1029/2009GL039825, 2009.

Wunch, D., Toon, G. C., Blavier, J.-F. L., Washenfelder, R. A., Notholt, J., Connor, B. J., Griffith, D. W., Sherlock, V., and Wennberg, P. O.: The total carbon column observing network, Philosophical Transactions of the Royal Society of London A: Mathematical, Physical and 670 Engineering Sciences, 369, 2087–2112, https://doi.org/10.1098/rsta.2010.0240, 2011.